Materials Today Bio 28 (2024) 101179

Contents lists available at ScienceDirect

Materials Today Bio

journal homepage: www.journals.elsevier.com/materials-today-bio

"Three birds, one stone" strategy of NIR-responsive CO/H_2S dual-gas Nanogenerator for efficient treatment of osteoporosis

Guoyu Yang [a], Jing Ye [a], Jingcheng Wang [a], Huijie Liu [b], Yanli Long [b], Junkai Jiang [b], Xinxin Miao [a], Jianjian Deng [a], Tianlong Wu [a], Tao Li [a], Xigao Cheng [a,**], Xiaolei Wang [b,*]

[a] Department of Orthopedics, the Second Affiliated Hospital, Jiangxi Medical College, Nanchang University, Nanchang, Jiangxi, 330088, PR China
[b] The National Engineering Research Center for Bioengineering Drugs and the Technologies, Institute of Translational Medicine, Nanchang University, Nanchang, Jiangxi, 330088, PR China

ARTICLE INFO

Keywords:
Near-infrared light
Upconversion nanoparticles
Carbon monoxide
Hydrogen sulfide
Osteoporosis

ABSTRACT

Osteoporosis (OP), the most prevalent bone degenerative disease, has become a significant public health challenge globally. Current therapies primarily target inhibiting osteoclast activity or stimulating osteoblast activation, but their effectiveness remains suboptimal. This paper introduced a "three birds, one stone" therapeutic approach for osteoporosis, employing upconversion nanoparticles (UCNPs) to create a dual-gas storage nanoplatform (UZPA-CP) targeting bone tissues, capable of concurrently generating carbon monoxide (CO) and hydrogen sulfide (H_2S). Through the precise modulation of 808 nm near-infrared (NIR) light, the platform could effectively control the release of CO and H_2S in the OP microenvironment, and realize the effective combination of promoting osteogenesis, inhibiting osteoclast activity, and improving the immune microenvironment to achieve the therapeutic effect of OP. High-throughput sequencing results further confirmed the remarkable effectiveness of the nanoplatform in inhibiting apoptosis, modulating inflammatory response, inhibiting osteoclast differentiation and regulating multiple immune signaling pathways. The gas storage nanoplatform not only optimized the OP microenvironment with the assistance of NIR, but also restored the balance between osteoblasts and osteoclasts. This comprehensive therapeutic strategy focused on improving the bone microenvironment, promoting osteogenesis and inhibiting osteoclast activity provides an ideal new solution for the treatment of metabolic bone diseases.

1. Introduction

With the aging of the global population, the prevalence of osteoporosis (OP) continues to rise, and it has become a major medical problem that seriously endangers human health and poses enormous socioeconomic challenges [1]. As a systemic bone metabolic disease, its core features include decreased bone mineral density and deterioration of bone tissue microarchitecture, resulting in increased bone fragility and fracture risk [2]. The development of this disease is mainly caused by dysfunction between various types of osteoblasts and immune cells in the bone microenvironment, resulting in an imbalance between bone formation and bone resorption [3]. Among them, osteoclasts play a key role in the development of OP, as they are not only responsible for bone resorption, but also for destroying bone minerals and collagen by secreting acids and catabolic enzymes [4,5], which in turn leads to severe bone mineral loss. Although osteoblast-mediated compensatory formation and mineralization of the bone matrix mitigate this loss to some extent, the inflammatory microenvironment limits its remineralization and repair during OP development [6]. The current clinical treatment of OP relies on the application of antiresorptive and pro-osteosynthesis drugs, but the off-target effect and accompanying side effects of these drugs limit their widespread use [7,8].

In recent years, nanomaterials have been widely used to carry various drug molecules, active substances, vesicles, or nucleic acids, regulating bone homeostasis to ameliorate OP symptoms [9–11]. Nevertheless, a considerable number of treatment strategies have the following two representative limitations: (1) Although nanomaterials with therapeutic components enable continuous drug release, the risk of burst release and subsequent elimination by the immune response hinders controllable and precise treatment. (2) The functions of the loaded

* Corresponding author.
** Corresponding author.
E-mail addresses: Ndefy12160@ncu.edu.cn (X. Cheng), wangxiaolei@ncu.edu.cn (X. Wang).

https://doi.org/10.1016/j.mtbio.2024.101179
Received 7 May 2024; Received in revised form 9 July 2024; Accepted 27 July 2024
Available online 6 August 2024
2590-0064/© 2024 The Authors. Published by Elsevier Ltd. This is an open access article under the CC BY-NC-ND license (http://creativecommons.org/licenses/by-nc-nd/4.0/).

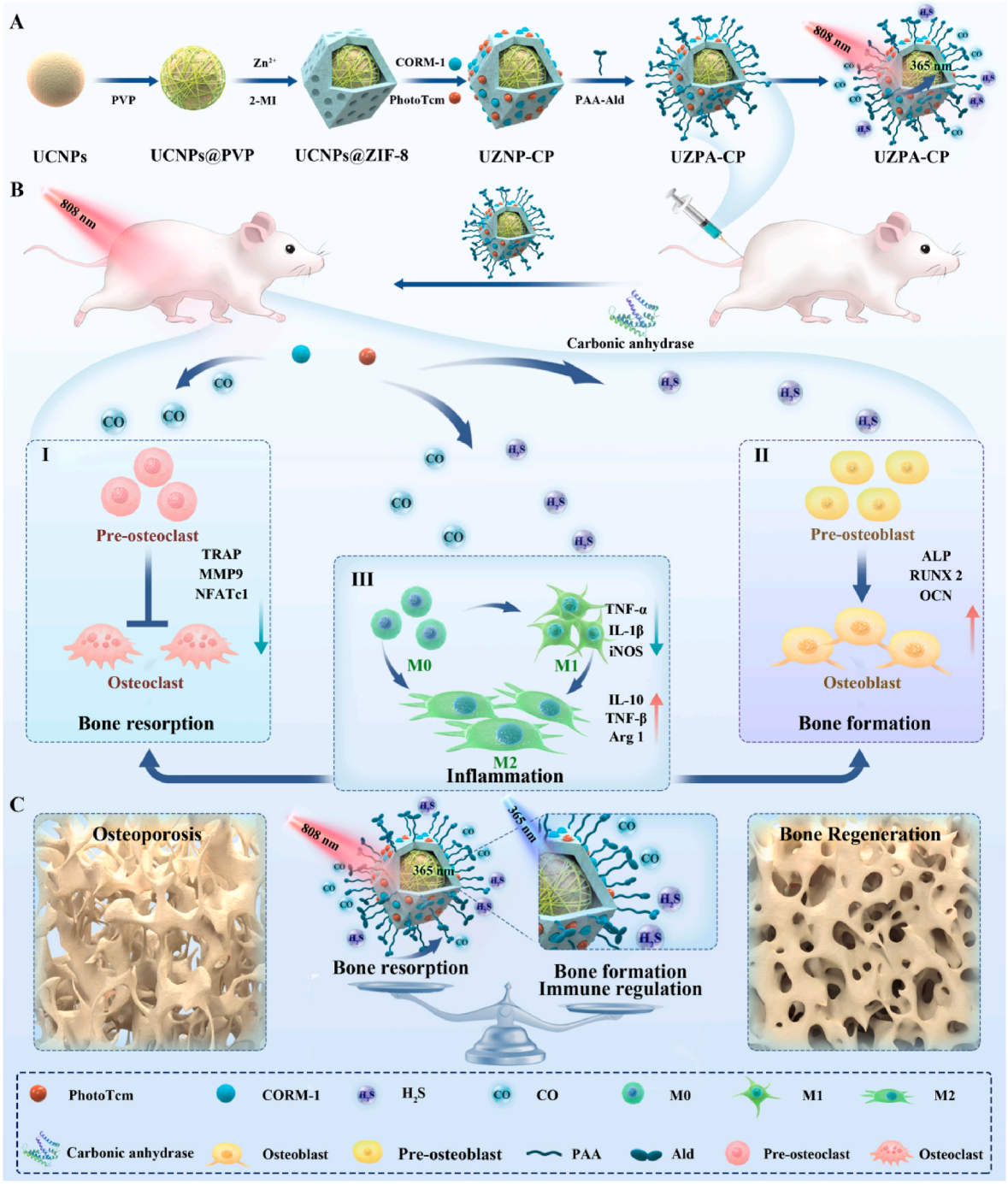

Scheme 1. Schematic representation of the synthesis and working principle of the bone-targeting gas storage nanoplatform (UZPA-CP) under 808 nm NIR light for regulating bone immune microenvironment to treat OP. (A) Synthesis of UZPA-CP. (B) Mechanism of OP treatment with UZPA-CP in mice: (I) CO released under 808 nm NIR irradiation suppresses the formation of osteoclasts. (II) H_2S released under 808 nm NIR exposure enhances the osteogenic differentiation of pre-osteoblast. (III) Under 808 nm NIR irradiation, the gas storage nanoplatform fostered the transition of macrophages from M1 to M2 phenotype, enhancing the immune microenvironment, and thereby actively contributing to the promotion of osteoblasts and suppression of osteoclasts. (C) Under 808 nm NIR irradiation, UZPA-CP could on-demand targeted delivery of CO and H_2S to reverse osteoporosis by enhancing osteoblast differentiation, suppressing osteoclast formation and modulating the immune microenvironment.

therapeutic agents are quite limited, focusing only on increasing osteoblast activity or suppressing osteoclast activity, without adequately addressing the specific microenvironment of OP. Hence, it is imperative to develop a multi-functional nanoplatform capable of precisely and on-demand release, as well as regulating the OP microenvironment to treat OP more effectively.

Gas molecules, due to their small size, rapid metabolism and involvement in numerous intracellular signaling pathways, have broad prospects in disease diagnosis and treatment [12,13]. Carbon monoxide (CO), as one of the earliest-discovered endogenous gases, has demonstrated potent anti-inflammatory and immune-regulatory functions [14–16]. Hydrogen sulfide (H_2S), discovered as the third gasotransmitter, plays a significant role in various physiological and pathological processes, notably in regulating bone homeostasis [17,18].

Theoretically, if CO and H_2S can be delivered accurately into the bone tissue at the same time and released in a controlled manner, not only the anti-inflammatory effect of CO as well as the osteogenic properties of H_2S can be utilized, but also the advantages of both can be incorporated to optimize the OP immune microenvironment, resulting in a comprehensive therapeutic effect of "1 + 1 > 2". Unfortunately, the controlled release of CO and H_2S is difficult to be realized within the op microenvironment simultaneously. Due to the temporal and spatial control flexibility of light sources, they have always been used to stimulate the production of gases [19]. However, the majority of CO and H_2S donors developed so far require excitation by blue-violet light (365 nm), which has limited tissue penetration and poses risks of skin damage or carcinogenesis with long-term exposure, constraining their use *in vivo* [20,21]. Near-infrared (NIR) light, with its higher biocompatibility and deeper tissue penetration, has been widely used in the treatment of various diseases [22]. Since the therapeutic window of NIR light lies within the 650−1100 nm range, it is necessary to develop a light conversion carrier that can transform low-energy NIR light into high-energy blue-violet light to effectively stimulate CO/H_2S donors. Upconversion nanoparticles (UCNPs), a type of light conversion nanocarrier that alters emission wavelengths through the doping of rare-earth elements, can transform NIR light into various wavelengths (ultraviolet, blue, green, red, *etc*.) of light, and are extensively used in treating deep-seated diseases such as tumors, thrombosis, and depression [23–26]. In our previous research, we had successfully combined UCNPs with mesoporous silica to achieve the controlled release of a single gas (nitric oxide) in treating thrombosis [27]. However, when applying this technology to the treatment of OP, we still faced issues including low loading efficiency and limited functionality of the single gas molecule, which prevented us from simultaneously and effectively improving the reduction of osteogenic capacity, the enhancement of osteoclast activity and the accompanying inflammatory microenvironment during the progression of OP.

In this work, we constructed a NIR-responsive gas storage nanoplatform (UZPA-CP) capable of precisely targeted and controlled delivery of dual gases (Scheme 1), which offered the following advantages: (1) Demand-driven, precise control release of gas molecules: The use of neodymium ions (Nd^{3+})-doped UCNPs converted NIR light with good tissue penetration into blue-violet light required for activating gas donors, facilitating the on-demand release of gas therapeutics; (2) High loading efficiency: The encapsulation of zeolitic imidazolate framework-8 (ZIF-8) provided UCNPs with a higher specific surface area, enhancing their capacity to simultaneously load two types of donors and making treatment more efficient; (3) Low off-target effects: By a simple and cost-effective method, polyacrylic acid-alendronate sodium (PAA-Ald, PA) was used to modify the surface of UZNP-CP, resulting in a UZPA-CP specifically targeting bone tissue and ensuring accurate concentration of dual gas molecules around the bone tissue requiring treatment; (4) Outstanding biocompatibility: The H_2S donor (PhotoTcm) in UZPA-CP, activated by light source/OP microenvironment dual stimuli, produced carbonyl sulfide (COS) under blue-violet light exposure, which required further hydrolysis by carbonic anhydrase (CA) secreted by osteoclasts in the OP microenvironment to generate H_2S. The sequential release of CO and H_2S efficiently mitigated cellular damage. More importantly, under 808 nm NIR irradiation, the blue-violet light formed by the light conversion nanocarrier was ultimately absorbed by the gas donors, minimizing the potential harm of high-energy light; (5) Multifunctionality: UZPA-CP combined the effects of CO in suppressing osteoclast activity with H_2S in enhancing osteogenic differentiation. It further effectively modulated the bone immune microenvironment, facilitating the differentiation of osteoblasts in inflammatory conditions, thus compensating for the deficiencies inherent in single-gas functionalities.

In conclusion, under the irradiation of 808 nm NIR, UZPA-CP demonstrated capabilities like enhancing bone formation, suppressing bone resorption, and modulating the immune microenvironment. This gas storage nanoplatform uniquely accomplished the targeted delivery of dual endogenous gases to the systemic bone microenvironment, offering a comprehensive therapeutic strategy for OP.

2. Materials and methods

2.1. Materials

Yttrium (III) acetate hydrate ($Y(CH_3CO_2)_3{\cdot}xH_2O$, 99.9 %), ytterbium (III) acetate hydrate ($Yb(CH_3CO_2)_3{\cdot}xH_2O$, 99.9 %), neodymium(III) acetate hydrate ($Nd(CH3CO_2)_3{\cdot}xH_2O$, 99.9 %), thulium (III) acetate hydrate ($Tm(CH_3CO_2)_3{\cdot}xH_2O$, 99.9 %), 1-octadecene (ODE, 90.0 %), oleic acid (OA, 90.0 %), nitrosonium tetrafluoroborate ($NOBF_4$), polyvinylpyrrolidone (PVP, Mw = 40,000), hydroxyapatite (HAP), dexamethasone (≥98 %), ascorbic acid (≥98 %), β-glycerophosphate, *o*-nitrobenzyl alcohol, bovine hemoglobin (Hb, ≥90 %), ammonium fluoride (NH_4F, 98 %), *p*-fluorophenylisothiocyanate, tetrahydrofuran (THF) and lipopolysaccharide (LPS) were purchased from Sigma. Cyclohexane, absolute ethanol, methanol, 2-methylimidazole (2-MI), Alendronate sodium trihydrate (Ald), polyacrylic acid (PAA, Mw ≈ 2000), 4-(4,6-Dimethoxy-1,3,5-triazin-2-yl)-4-methylmorpholinium chloride (DMTMM, 97 %), N,N-dimethylformamide (DMF), sodium bisulfite ($NaHSO_3$, ≥82 %), isopropyl alcohol, hexane, sodium hydroxide (NaOH, 97 %) and sodium nitrite ($NaNO_2$, 99.9 %) were purchased from Aladdin. Zinc nitrate hexahydrate ($Zn(NO_3)_2{\cdot}6H_2O$, 99 %) was purchased from Sinopharm Chemical Reagent Co., Ltd. All chemicals were used without any further purification.

2.2. Characterization

The morphology, energy-dispersive X-ray spectroscopy, and elemental mapping images of the as-synthesized nanoparticles were observed by field emission transmission electron microscope (TEM, Tecnai G2 20, Thermo Fisher Scientific, US) and field emission scanning electron microscopy (SEM, Zeiss Sigma 300, Germany). The X-ray diffraction (XRD, D8A A25 X, Bruker, Germany) was used to test the crystal structure of the samples. The various nanoparticles' chemical compositions were characterized by Fourier-transform infrared (FT-IR) spectra (Nicolet iS20, Thermo Fisher Scientific, US). The Zeta potentials of various nanoparticles were measured using zeta potential instrument (Zetasizer Nano ZS90, Malvern, UK). The element information of samples was measured by X-ray photoelectron spectroscopy (XPS, Thermo Fisher Scientific K-Alpha, USA). Near-infrared (NIR) laser was produced using 808 nm multimode fiber-coupled laser (LOS-BLD-0808-5W–C/P, max: 5 W, Hi-Tech Optoelectronics, China) and 980 nm multimode fiber-coupled laser (LOS-BLD-0980-5W–C/P, max: 5 W, Hi-Tech Optoelectronics, China). The upconversion luminescence (UCL) spectra were measured by fluorescence spectrophotometer (FL970, Techcomp, China). The UV–visible (UV–vis) absorption spectra were collected by UV-2600 Spectrophotometer (Shimadzu, Japan). All the fluorescence measurements were conducted by inverted fluorescence microscopy (Axio Observer, Zeiss, Germany). The optical images were obtained by optical microscope (Axio Lab.A1, Zeiss, Germany). The absorbances and optical density (OD) values were measured by microplate reader of VICTOR Nivo 3S (PerkinElmer, US). Skeletal analyses were performed using a micro-CT system (Scanco Medical).

2.3. Synthesis of UCNP nanocrystals

The core-shell-shell structure of $NaYF_4$:Yb/Tm@$NaYF_4$:Nd/Yb@$NaYF_4$ upconversion nanoparticles (UCNPs) was synthesized *via* the hydrothermal method as described previously [28]. Briefly, the core nanocrystals of β-$NaYF_4$:25%Yb/0.5%Tm were synthesized at first. 0.745 mmol of $Y(CH_3CO_2)_3{\cdot}xH_2O$, 0.25 mmol of $Yb(CH_3CO_2)_3{\cdot}xH_2O$ and 0.005 mmol of $Tm(CH_3CO_2)_3{\cdot}xH_2O$ were added into the solution containing 15 mL of ODE and 6 mL of OA in a 100 mL three-necked flask. Then, the mixture was heated to 150 °C and maintained for 60 min to

form a clear solution. Upon cooling to room temperature, 10 mL of methanol solution containing 4 mmol of NH_4F and 2.5 mmol of NaOH was added to the solution. Afterward, the mixture was heated to 50 °C and maintained for 30 min. The reaction vessel was then heated to 120 °C for 30 min to remove methanol and subsequently heated to 300 °C under the argon atmosphere, maintaining for 90 min. After cooling down to room temperature, 10 mL of ethanol was added to precipitate the UCNPs. Finally, the precipitated UCNPs were washed with ethanol and dispersed in 5 mL of cyclohexane.

The core-shell UCNPs were synthesized with the same coprecipitation procedure. Typically, 0.35 mmol of $Y(CH_3CO_2)_3{\cdot}xH_2O$, 0.05 mmol of $Yb(CH_3CO_2)_3{\cdot}xH_2O$ and 0.1 mmol of $Nd(CH_3CO_2)_3{\cdot}xH_2O$ were added into the solution containing 15 mL of 1-octadecene (ODE) and 6 mL of oleic acid (OA) in a 100 mL three-necked flask. Then the mixture was heated to 150 °C for 30 min to form a clear solution. Next, the prepared β-$NaYF_4$:25%Yb/0.5%Tm solution was added into this mixture, and the mixed solution was stirred at 70 °C for 20 min. Upon cooling down to room temperature, 10 mL of methanol solution containing 4 mmol of NH_4F and 2.5 mmol of NaOH were added to the solution and stirred at 50 °C for 30 min. The reaction vessel was then heated to 120 °C for 30 min to remove methanol and subsequently heated to 300 °C under the argon atmosphere, maintaining for 90 min. After cooling to room temperature, the core-shell nanocrystals were precipitated by ethanol and washed with methanol, dispersing in 5 mL of cyclohexane.

The synthesis of core-shell-shell nanocrystals was as outlined for $NaYF_4$:20%Nd/10%Yb shell growth mentioned above, except Y $(CH_3CO_2)_3{\cdot}xH_2O$, $Yb(CH_3CO_2)_3{\cdot}xH_2O$ and $Nd(CH_3CO_2)_3{\cdot}xH_2O$ were replaced by 0.5 mmol of $Y(CH_3CO_2)_3{\cdot}xH_2O$.

2.4. Synthesis of UCNPs@PVP

By modifying with PVP, oily UCNPs were transformed into water-soluble UCNPs. Initially, the oleic acid on the surface of UCNPs was eliminated using $NOBF_4$ ligand exchange, then proceeded with PVP modification [29]. In detail, a mixture of 5 mL UCNPs solution (concentration 5 mg mL^{-1} in cyclohexane) and 5 mL $NOBF_4$ DMF solution (0.01 M) was stirred gently at room temperature for 1 h. Once the solution separated into layers, the cyclohexane layer was discarded, and an equal volume of isopropanol and n-hexane (1:1 v/v) was added to the rest, then centrifuged to eliminate the supernatant and re-dispersed the precipitate in DMF. Then, the solution was introduced into an aqueous solution with 100 mg PVP, stirred intensely for 12 h at room temperature, then centrifuged at 11,000 rpm for 10 min, washed the precipitate with water and methanol, and ultimately re-dispersed in methanol.

2.5. Synthesis of UCNPs@ZIF-8

The method for synthesizing UCNPs@ZIF-8 was adapted from the original procedure with some modifications [30]. 9 mL of Zn $(NO_3)_2{\cdot}6H_2O$ (25 mM, in methanol/DMF) was mixed with 1 mL of UCNPs@PVP solution and stirred for 2 h, followed by adding 10 mL of 2-MI (25 mM, in methanol/DMF), and then left undisturbed at 40 °C for 24 h. The product was collected by centrifugation, washed several times with methanol, and finally dissolved in 1 mL of ethanol.

2.6. Synthesis of PhotoTcm

The *o*-nitrobenzyl alcohol species (1.0 equiv.) was combined with *p*-fluorophenyl isothiocyanate (1.0 equiv.) in anhydrous THF (15 mL) at 0 °C, followed by the addition of NaH (60 % in paraffin liquid, 1.25 equiv). The resultant mixture was stirred at 0 °C for 20 min, after which the ice bath was removed, and the reaction mixture was stirred at room temperature until the completion of the reaction indicated by thin-layer chromatography (TLC). The reaction was quenched by adding brine (30 mL), and the aqueous solution was extracted with ethyl acetate (3 × 15 mL). The organic layers were combined, dried over magnesium sulfate ($MgSO_4$), and evaporated under vacuum. The crude product was purified by column chromatography.

2.7. Synthesis of UZNP-CP

UZNP-CP was obtained by loading CORM-1 and PhotoTcm into UCNPs@ZIF-8. First, 5 mg of UCNPs@ZIF-8 was combined with different masses of CORM-1 and PhotoTcm (with a 1:1 M ratio in 5 mL ethanol), setting the mass ratios of UCNPs@ZIF-8 to CORM-1 and PhotoTcm at 0.5:1, 1:1, 2:1, and 5:1. The mixture was stirred in the dark for 12 h and then centrifuged at 11,000 rpm for 10 min to collect UZNP-CP. Following this, the drug loading under different mass ratios was calculated by analyzing the remaining amounts of CORM-1 and PhotoTcm in the supernatant. The gathered UZNP-CP needed to be washed thrice with water and preserved at 4 °C. Lastly, the drug loading was determined using the standard curves of CORM-1 and PhotoTcm. The formula for calculating the drug loading rate was as follows:

$$\text{Drug loading rate } (\%) = \frac{\text{weight of loaded CORM–1/PhotoTcm}}{\text{weight of UZNP–CP}} \times 100\%$$

2.8. Synthesis of UZPA-CP

First, an appropriate amount of PAA and Ald was added to a borate buffer solution and stirred until completely dissolved to facilitate the binding between PAA and Ald. Following 10 min of stirring, DMTMM (0.055 g, 0.2 mmol) was incorporated into 20 mL of borate buffer solution (0.1 M, pH 8.5), and then the pH was adjusted to 7.5 using 2 M NaOH. Under conditions of constant stirring, the reaction was carried out for 24 h. Afterward, the product was purified through dialysis and freeze-dried, yielding a white foamy substance, PAA-Ald. Following this, 20 mg of PAA-Ald was dissolved in 100 mL of deionized water with 100 mg of UZNP-CP, and the mixture was stirred overnight. The product was then centrifuged and washed with deionized water, followed by vacuum drying to acquire the final powdered product of UZPA-CP [25].

2.9. NIR-responsive CO release detection

We prepared a co-saturated solution with phosphate buffered saline (PBS, pH 7.4) and carbon monoxide (CO), and used it immediately. $NaHSO_3$ was employed to reduce Hb, resulting in the formation of oxyferrous-Hb. In a dark and anaerobic environment, 2 mg mL^{-1} of UZPA-CP was introduced into a PBS buffer with 10 μM oxidized ferrous hemoglobin. Following 808 nm NIR laser irradiation (1.5 W cm^{-2}), the absorbance of solution at various time points was detected using a UV–vis spectrophotometer, and the quantity of CO released by UZPA-CP was calculated using the formula from prior research.

2.10. NIR-responsive H_2S release detection

The release of H_2S was measured using an hydrogen sulfide (H_2S) assay kit, CA solution was added to the UZPA-CP solution followed by irradiation with 808 nm NIR laser (1.5 W cm^{-2}), and the generation of H_2S was periodically monitored. During this process, the produced H_2S reacted with N,N-dimethyl-*p*-phenylenediamine and ammonium ferric sulfate to form methylene blue, which exhibited its maximum absorption peak at 665 nm. The concentration of H_2S could be calculated by determining the absorbance of methylene blue. Specifically, 100 μL of liquid sample was added to 1 mL of Extraction Solution I, centrifuged at 12,000 g at 4 °C for 10 min, then 0.8 mL of the supernatant was taken, 0.15 mL of Extraction Solution II was added, and centrifuged at 12,000 g at 4 °C for 10 min. The supernatant was taken, while Reagent I and Reagent II were added from the detection kit, fully mixed, and stood at room temperature for 10 min. The absorbance was measured at 665 nm and substituted into the standard equation $y = 0.0020x - 0.0633$, $R^2 = 0.9951$, to calculate the quantity of H_2S.

2.11. Cell culture

This research utilized the mouse monocyte macrophages (RAW 264.7) cells and mouse embryonic osteogenic precursor (MC3T3-E1) cells. The RAW 264.7 cells were sourced from Wuhan PunoSai Life Science Co., Ltd. in China, and the MC3T3-E1 cells were provided by the Chinese Academy of Medical Sciences, Beijing. Both of cell types were cultured in Dulbecco's Modified Eagle's Medium (DMEM), which included 10 % fetal bovine serum (FBS) and penicillin/streptomycin (PS). The cells were cultured under conditions of 37 °C and 5 % Carbon dioxide (CO_2) in a constant temperature and humidity incubator.

2.12. Detection of intracellular CO

Intracellular CO was detected using the CO probe CAY10733. Initially, RAW 264.7 cells were seeded in a 12-well plate at a density of 8×10^4 cells per well. After the cells adhered, fresh culture medium containing UZPA-CP was added, and the cells were incubated for 6 h. The cells were then treated for 30 min with a 1 μM concentration of CAY10733 solution. Post-treatment, the cells were exposed to 808 nm NIR laser (power density 1.5 W cm^{-2}) for 5 min. Lastly, the cell nuclei were stained with Hoechst 33342, and stained cells were viewed using an inverted fluorescence microscope.

2.13. Detection of intracellular H_2S

Intracellular H_2S was detected using the H_2S probe WSP-1. Initially, MC3T3-E1 cells were seeded in a 12-well plate at a density of 8×10^4 cells per well. After the cells adhered, a fresh culture medium containing UZPA-CP and CA solution was added and incubated for 6 h. Thereafter, the cells were treated with a 100 μM solution of WSP-1 for 30 min. Subsequently, the cells were exposed to 808 nm NIR laser (power density 1.5 W cm^{-2}) for 5 min. Post-irradiation, the cell nuclei were stained with Hoechst 33342, and the stained cells were examined using an inverted fluorescence microscope.

2.14. Cell Viability

Cell cytotoxicity of UZPA-CP nanoparticles was evaluated using a CCK-8 assay kit from Beyotime, China. The RAW 264.7 cells and MC3T3-E1 cells were grown at a density of 5×10^3 cells per well. The cells were exposed to different concentrations of UZPA-CP nanoparticles for periods of 1, 2 and 3 days. Post-treatment, each well received 100 μL of DMEM with 10 μL of CCK-8 solution, followed by incubation at 37 °C for 1 h, and finally, the absorbance at 450 nm was assessed.

2.15. Live/dead cell staining

The two cell types were plated at a density of 3×10^4 cells per well on a 24-well plate. Following cell attachment, the existing culture medium was substituted with a complete medium containing 100 μg mL^{-1} UZPA-CP, and the cells were co-incubated for 24 h. After the incubation period, the culture medium was removed, and each well was filled with a serum-free medium containing 5 μL Calcein-AM and PI, incubating for 30 min. The cells were then washed twice with PBS and observed and imaged using an inverted fluorescence microscope.

2.16. Hemolytic test

Initially, blood was extracted from mice and then centrifuged at a speed of 1500 rpm for 15 min. Red blood cells were diluted with sterile saline, and then 100 μL of the diluted suspension was mixed with 1.1 mL saline solution and deionized water as the negative control and the positive control, respectively. Additionally, the same volume of red blood cell suspension was mixed with 1.1 mL various concentrations of UZPA-CP solution to form the experimental group. Subsequently, all Eppendorf tubes were incubated in a 37 °C water bath for 1 h. After incubation, the supernatant was collected, and the absorbance at 540 nm was measured using an enzyme-linked immunosorbent assay to calculate the hemolysis rate.

2.17. Evaluation of osteogenic activity

Osteogenic activity was determined using western blot (WB), alkaline phosphatase (ALP) staining, alizarin red (ARS) staining and quantitative reverse transcription-polymerase chain reaction (qRT-PCR). The MC3T3-E1 cells were cultivated in osteogenic induction medium comprising 50 ng/mL ascorbic acid, 10 mM β-glycerophosphate and 10 nM dexamethasone, supplemented with various nanoparticles and CA. Throughout the incubation period, the induction medium was refreshed every 3 days, with the culture extending for both 7 and 14 days. Following a 7-day culture period, cells were fixed with 4 % paraformaldehyde, washed thrice with PBS, and ALP activity was assessed using an ALP staining kit. Following a culture period of 14 days, the cells were stained using ARS staining solution. Then, images were captured under a microscope, and a semi-quantitative analysis of the osteogenic effect was conducted using Image J software. WB assay was employed to detect osteogenesis-related proteins such as osteopontin (OPN) and ALP. Additionally, qRT-PCR was utilized to assess the expression levels of osteogenesis-related genes. Details of the primers used could be found in Table S1 in the Supporting Information.

2.18. Polarization and inflammatory gene expression in RAW 264.7 cells

The polarization state (M1/M2) of RAW 264.7 cells was determined using flow cytometry, immunofluorescence, and qRT-PCR. RAW 264.7 cells were plated at a density of 1×10^6 cells per well in 6-well plates and cultured for 24 h. Concurrently, treatment with various samples, CA and 1 μg mL^{-1} LPS was carried out for 24 h. Initially, the polarization state of RAW 264.7 cells was evaluated using flow cytometry. Fluorescently-tagged CD86 antibody (Servicebio, China) for M1 marking and CD206 antibody (Servicebio, China) for M2 marking were applied, with staining conducted at room temperature for 1 h. Nuclei were counterstained with 4',6-diamidino-2-phenylindole (DAPI). Finally, images were collected using an inverted fluorescence microscope. Total RNA was extracted from the cells using Trizol reagent (Beyotime, China), and cDNA was synthesized from the isolated RNA by reverse transcription. The expression levels of relevant inflammatory genes were detected by qRT-PCR.

2.19. Osteoclast formation assay

Osteoclast activity was evaluated using anti-tartrate acid phosphatase (TRAP) staining and qRT-PCR. Initially, RAW 264.7 cells were seeded at a density of 3×10^4 cells per well into 48-well plates and induced with RANKL and M-CSF. Concurrently, the cells were co-cultured with various nanomaterials for 5 days. Subsequently, the cells were stained with TRAP, and TRAP-positive osteoclasts, indicated by wine-red cytoplasm, were observed under a microscope (Zeiss, Germany). In addition, the expression levels of osteoclast-related genes were measured using qRT-PCR.

2.20. Conditional osteogenic differentiation experiment

RAW 264.7 cells were seeded at a density of 1×10^5 cells/dish in 60 mm culture dishes. After the cells adhered, the original medium was replaced with high-glucose medium containing 1 μg mL^{-1} LPS. After 24 h of stimulation, the supernatant was collected and cell debris and impurities in the medium were removed by high-speed centrifugation. Subsequently, the obtained medium was mixed with osteogenic induction medium in a 1:1 ratio to prepare conditioned osteogenic induction medium, which was then stored at −20 °C for later use. MC3T3-E1 cells

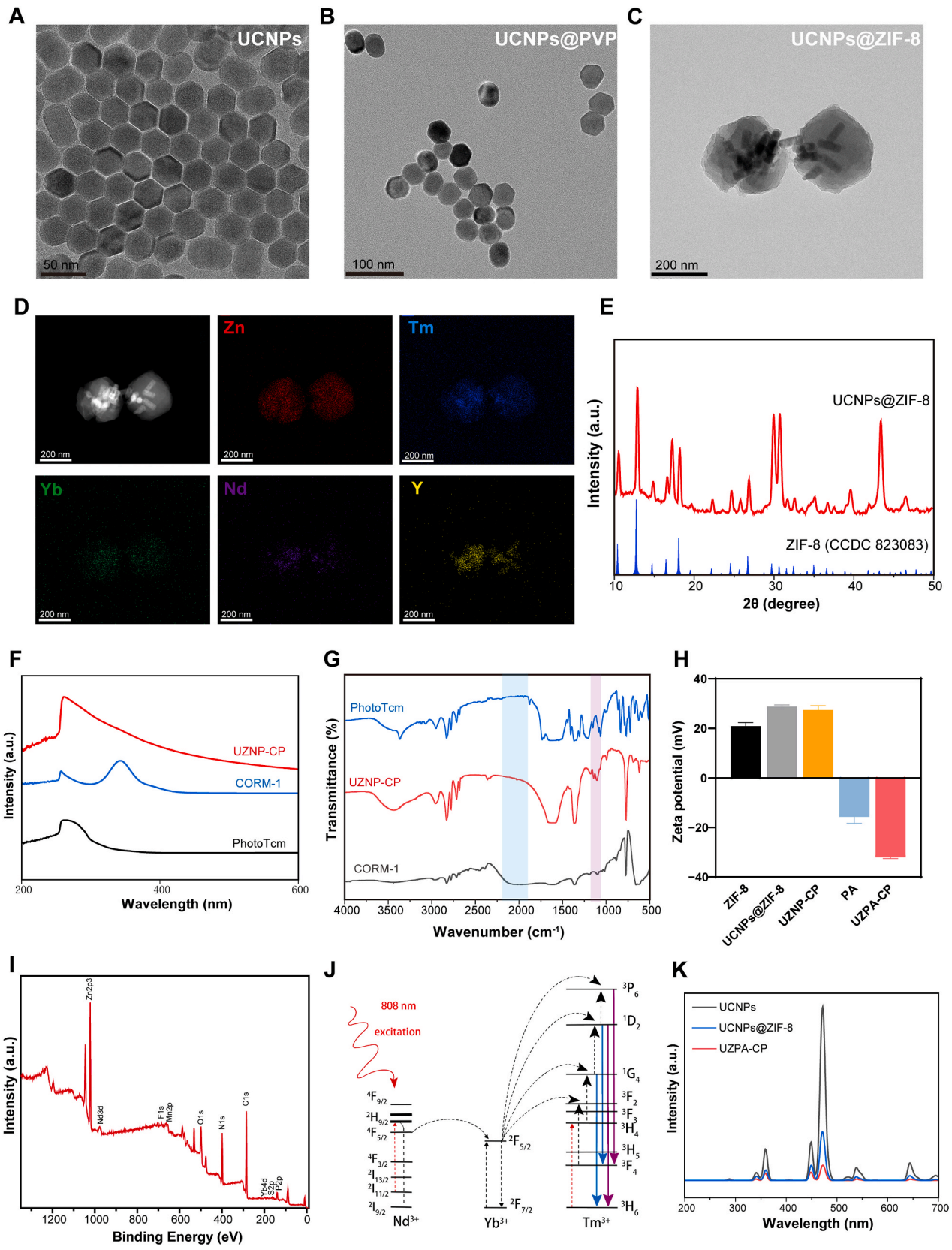

Fig. 1. Synthesis and characterization of UZPA-CP. (A–C) TEM images of UCNPs, UCNPs@PVP, and UCNPs@ZIF-8 (from left to right). (D) Mapping images of UCNPs@ZIF-8. (E) XRD pattern of UCNPs@ZIF-8. (F) UV–vis absorption spectra of PhotoTcm, CORM-1 and UZNP-CP solutions. (G) FT-IR spectra of PhotoTcm, UZNP-CP, and CORM-1 solutions. (H) Zeta potentials of ZIF-8, UCNPs@ZIF-8, UZNP-CP, PA, and UZPA-CP. (I) XPS spectrum of UZPA-CP. (J) Upconversion energy transfer diagram of Nd^{3+}, Yb^{3+} and Tm^{3+} under 808 nm NIR excitation. (K) UCL spectra of UCNPs, UCNPs@ZIF-8, and UZPA-CP. Data are mean ± sd (n ≥ 3).

were cultured with conditioned osteogenic induction medium containing the same concentration of various nanomaterials and CA, and the osteogenic activity of the cells was detected by ALP and ARS staining. In addition, the expression levels of osteogenic genes were detected by qRT-PCR, and the expression levels of related osteogenic proteins were detected by WB.

2.21. High-throughput sequencing and bioinformatics analysis

RAW 264.7 cells were treated with LPS and LPS + UZPA-CP + NIR. MC3T3-E1 cells were treated with medium and medium + UZPA-CP + NIR. Cells from different groups were collected, total RNA was extracted using TRIzol reagent (Beyotime, China), and transcriptome sequencing and bioinformatics analysis were conducted by OE Biotech Co., Ltd. (Shanghai, China).

2.22. Bone targeting capacity In vitro and In vivo

The affinity of UZPA-CP and non-targeted UZNP-CP for bone minerals was studied. 1 mg mL^{-1} of UZPA-CP and UZNP-CP were each incubated with 20 mg HAP (HAP particles) in 5 mL solution and stirred for varying times (0 min, 10 min, 30 min and 60 min). After the incubation period, the solution was centrifuged to precipitate HAP and its bound nanoparticles. The precipitate was washed several times with deionized water, dried in an oven, and characterized by SEM. For *in vivo* bone targeting, C57 mice (10 weeks old) were intraperitoneally injected with UZPA-CP and PBS, after various time intervals, the animals were euthanized, and their bones thoroughly exposed for imaging.

2.23. Animal experiment

All experiments were conducted in accordance with relevant guidelines and approved by the Ethics Committee of Nanchang University (NCULAE-20221228021). In brief, 10-week-old female C57 mice underwent ovariectomy using minimally invasive surgical techniques under aseptic conditions, while a sham operation was performed on six mice of the same batch. After four weeks, the mice were divided into four groups: Sham, OVX, OVX + UZPA-CP – NIR, and OVX + UZPA-CP + NIR, with 6 mice in each group. As previously described, equal amounts of nanomaterial or PBS were intraperitoneally injected every 2 days. Four weeks later, the mice were euthanized for bone analysis using micro-CT.

2.24. Micro-CT scanning

Post-euthanasia, bone tissues (the third lumbar vertebra and femur) were harvested and fixed in 10 % neutral buffered formalin. Micro-CT (Scanco Medical) was used to scan the microstructure of the third vertebral body and left femoral trabeculae, with software used to reconstruct the acquired images. Parameters of bone structure, including BMD, BS/TV, BV/TV, Tb.Sp and Tb.N, were ascertained by analyzing targeted regions.

2.25. Histological staining

Lumbar vertebrae and femurs were fixed in 10 % formalin buffer for a minimum of 48 h, then decalcified in 10 % ethylenediaminetetraacetic acid (EDTA) for a week. Specimens were embedded in paraffin and sectioned at 5 μm. Routine HE staining was performed to observe morphological changes in tissue and trabecular areas. Masson staining was conducted to assess new bone formation, while TRAP staining quantified the number of TRAP-positive osteoclasts in specified areas. Ultimately, immunofluorescence staining was used to determine the quantity of TNF-α and IL-10 positive cells in chosen regions. Semi-quantitative analysis of the above results was performed using Image J (Bethesda, USA).

2.26. Naming of materials

In our study, CORM-1 served as the CO donor, and PhotoTcm served as the H2S donor. Accordingly, we designated the material with only CORM-1 as UZPA-C, the material with only PhotoTcm as UZPA-P, and the material containing both donors as UZPA-CP. UZPA-CP + NIR denotes the material with both CO and H_2S donors, treated with additional NIR irradiation. Similarly, UZPA-C + NIR refers to the material with only the CO donor, also treated with NIR irradiation. UZPA-P + NIR refers to the material with only the H_2S donor, also treated with NIR irradiation.

2.27. Statistical analysis

The data were expressed as mean ± standard deviation (SD). Statistical analyses were conducted using one-way analysis of variance (ANOVA), and *t*-tests were carried out with GraphPad Prism 8.0. Statistical values of $^{*}p < 0.05$, $^{**}p < 0.01$, $^{***}p < 0.001$, $^{****}p < 0.0001$ were regarded statistically significant.

3. Results and discussion

3.1. Synthesis and characterization of UZPA-CP

In this study, hydrophobic UCNPs ($NaYF_4$:Yb/Tm@$NaYF_4$) with a core-shell structure stabilized by oleic acid were synthesized *via* the thermal decomposition method [28], with an average particle size of about 35 nm (Fig. 1A–S1 and S2). Subsequently, oleic acid on the surface of UCNPs was removed using the nitrosyl tetrafluoroborate ($NOBF_4$) ligand exchange technique, followed by hydrophilic modification with polyvinylpyrrolidone (PVP), resulting in UCNPs@PVP with a diameter of about 40 nm. Transmission electron microscopy (TEM) image confirmed that PVP modification did not alter the crystal structure of UCNPs (Fig. 1B). Subsequently, UCNPs@PVP was reacted with zinc nitrate hexahydrate and 2-methylimidazole to synthesize UCNPs@ZIF-8 [29,30]. The TEM and elemental mapping results of UCNPs@ZIF-8 confirmed its successful preparation, with a particle size of about 240 nm (Fig. 1C and D). X-ray diffraction (XRD) analysis showed that UCNPs@ZIF-8 had the same characteristic diffraction peaks as pure ZIF-8 (CCDC 823083), further confirming the successful encapsulation of ZIF-8 (Fig. 1E). Nitrogen adsorption-desorption experiments indicated that UCNPs@ZIF-8 had a specific surface area of about 1215.7 m^2/g (Fig. S3), suggesting that this composite material, due to its high specific surface area, had efficient drug encapsulation and loading capabilities [31]. We then synthesized the H_2S donor PhotoTcm. Fourier-transform infrared (FT-IR) spectroscopy and nuclear magnetic resonance hydrogen spectroscopy (^1H NMR) verified the successful synthesis of PhotoTcm (Fig. S4) [32]. Following this, the CO donor (CORM-1) and PhotoTcm were co-loaded onto UCNPs@ZIF-8, resulting in the formation of UZNP-CP. Ultraviolet–visible (UV–vis) spectroscopy analysis indicated enhanced absorption of UZNP-CP in the blue-violet light range (Fig. 1F). Additionally, the characteristic peaks of CORM-1 (Fig. 1G, blue region) and PhotoTcm (Fig. 1G, purple region) in the FT-IR spectra were both identified in UZNP-CP, further verifying its successful synthesis. According to the standard curves (Fig. S5), the maximum loading capacities of CORM-1 and PhotoTcm in UCNPs@ZIF-8 were about 15.35 % and 10.88 %, respectively. To endow UZNP-CP with bone-targeting capability, polyacrylic acid (PAA) was covalently modified onto sodium alendronate (ALD) to form PAA-ALD (PA), which was then adsorbed onto the UZNP-CP surface through electrostatic adsorption [25], creating the final bone-targeting gas storage nanoplatform UZPA-CP. The zeta potentials of ZIF-8, UCNPs@ZIF-8, UZNP-CP, PA, and UZPA-CP were measured. Notably, upon binding with PA, the positively charged UZNP-CP transformed into negatively charged UZPA-CP (about −32.39 mV) (Fig. 1H), confirming the successful modification with the bone-targeting ligand. X-ray

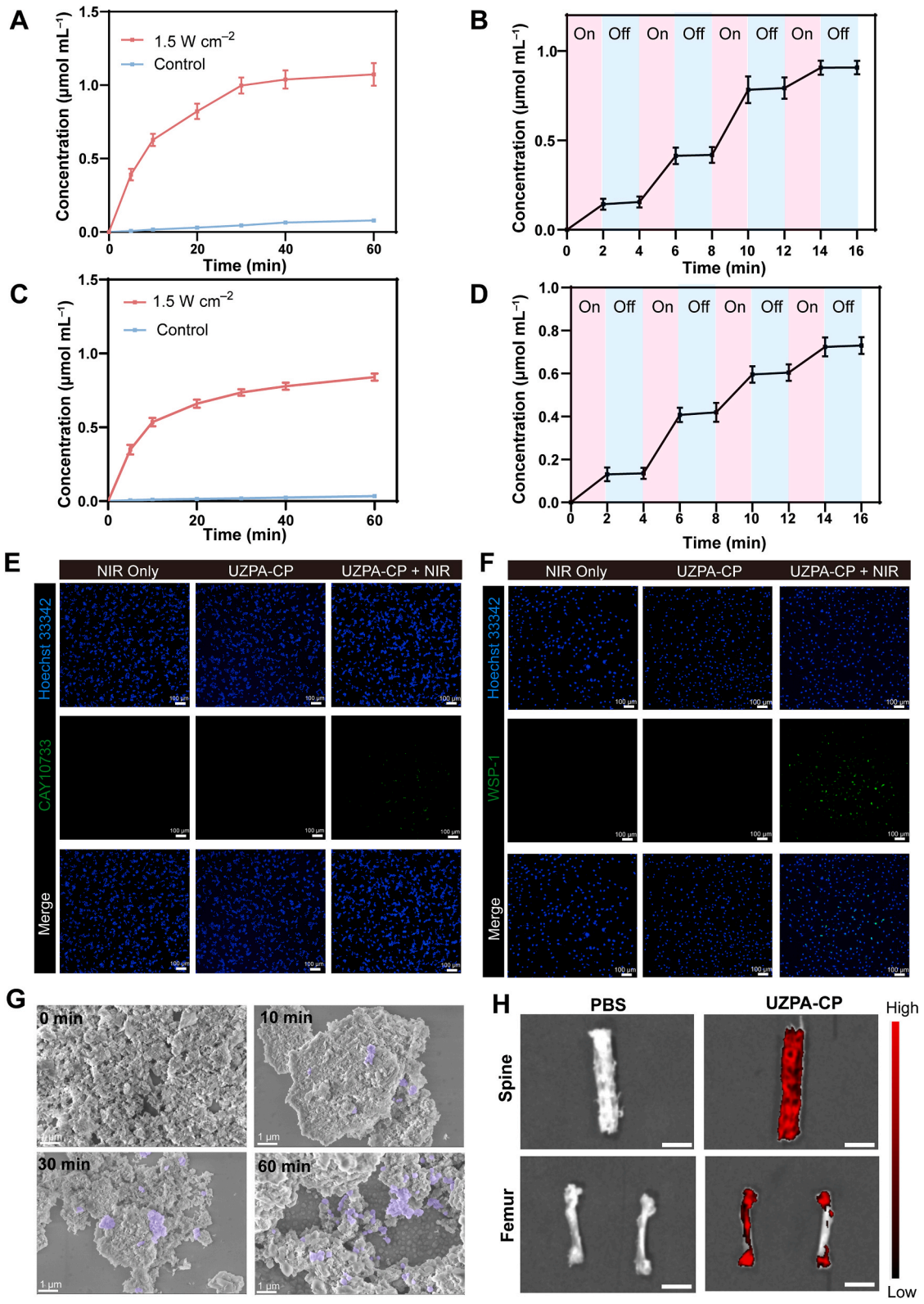

Fig. 2. Photoreactive and *in vitro* and *in vivo* targeting performance evaluation of UZPA-CP. (A) The release curve of CO under 808 nm NIR irradiation (1.5 W cm^{-2}). (B) On/off experiments of CO release under 808 nm NIR irradiation (1.5 W cm^{-2}). (C) The release curve of H_2S under 808 nm NIR irradiation (1.5 W cm^{-2}). (D) On/off experiments of H_2S release under 808 nm NIR irradiation (1.5 W cm^{-2}). (E) Fluorescent images of RAW 264.7 cells co-cultured with UZPA-CP with/without NIR irradiation (Hoechst 33342 and CY10733 fluorescent probes), scale bar = 100 μm. (F) Fluorescent images of MC3T3-E1 cells co-cultured with UZPA-CP with/without NIR irradiation (Hoechst 33342 and WSP-1 fluorescent probes), scale bar = 100 μm. (G) Representative SEM images of UZPA-CP targeting HAP at different time intervals. (H) Fluorescence imaging of the mouse skeleton 6 h after intraperitoneal injection of UZPA-CP material, scale bar = 0.5 cm. Data are mean ± sd (n ≥ 3).

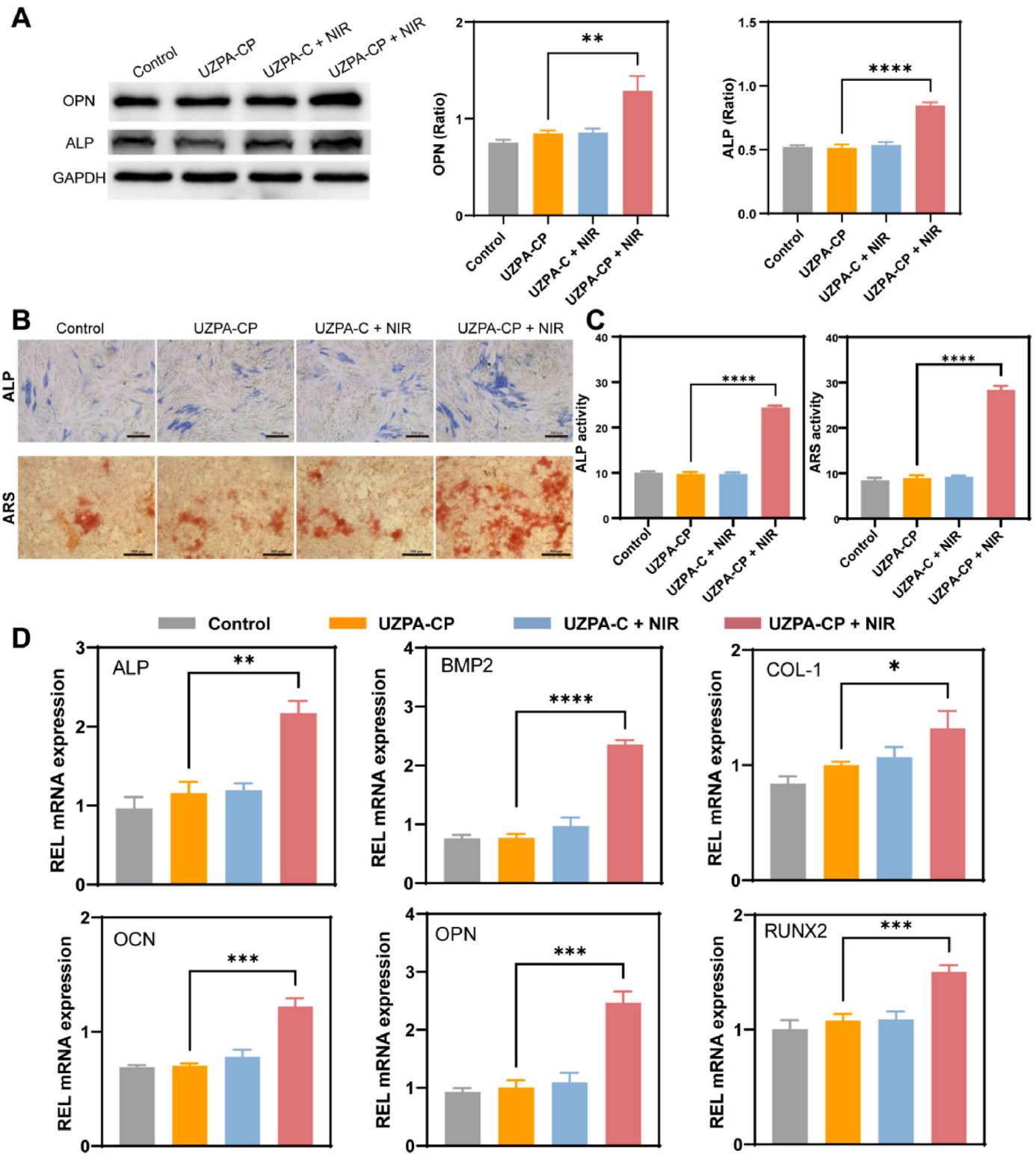

Fig. 3. Evaluation of the osteogenic ability of UZPA-CP. (A) WB analysis of osteogenic factors (OPN and ALP) protein levels in MC3T3-E1 cells and their quantitative results. (B) Images of ALP staining (scale bar = 200 μm) after co-culturing with MC3T3-E1 cells for 7 days and ARS staining (scale bar = 500 μm) after co-culturing for 14 days. (C) Quantitative results corresponding to ALP and ARS staining. (D) The mRNA expression of ALP, BMP2, COL-1, OCN, OPN and RUNX2 in MC3T3-E1 cells after co-culturing with MC3T3-E1 cells for 7 days. Data are mean ± sd (n ≥ 3), *$p < 0.05$, **$p < 0.01$, ***$p < 0.001$, ****$p < 0.0001$.

photoelectron spectroscopy (XPS) revealed the presence of representative elements such as manganese (Mn), sulfur (S), zinc (Zn), and phosphorus (P) in UZPA-CP (Fig. 1I), further confirming the successful modification with gas donors and the targeting ligand. All these results confirmed the successful construction of the bone-targeting gas storage nanoplatform. UCNPs, acting as energy donors, adopted a core-shell-shell structure sensitized by a neodymium/ytterbium/thulium ($Nd^{3+}/Yb^{3+}/Tm^{3+}$) cascade (Fig. 1J). Under 808 nm NIR excitation, the fluorescence emission spectrum of UCNPs displayed typical emission peaks , corresponding to electronic

transitions from $^3P_6$ to $^3F_4$, $^1D_2$ to $^3H_6$, $^1D_2$ to $^3F_4$ and $^1G_4$ to $^3H_4$, respectively (Fig. S6) [33,34]. The upconversion luminescence (UCL) spectral data showed that compared with unmodified UCNPs, the modification with PA and loading of donors significantly reduced the luminescence intensity (Fig. 1K). These results indicated effective fluorescence resonance energy transfer (FRET) within UZPA-CP and efficient absorption of blue-violet light by UZPA-CP.

3.2. In vitro Cytocompatibility and laser safety Assessment

The biosafety of nanomaterials is a prerequisite for their application *in vivo*. We initially assessed the *in vitro* biosafety of UZPA-CP using mouse embryonic osteogenic precursor cells (MC3T3-E1) and mouse monocyte macrophages (RAW 264.7) cells. Through cell counting kit-8 (CCK-8) assay and live/dead cell staining, it was determined that UZPA-CP exhibited good biocompatibility at a concentration of 100 μg mL^{-1} (Fig. S7), and similar results were also verified in erythrocyte hemolysis assay (Fig. S8). Therefore, in subsequent experiments, we set the concentration of nanomaterials used at 100 μg mL^{-1}. Furthermore, although the gas storage nanoplatform we used can be more effectively excited by 980 nm NIR, the absorption coefficient of water molecules in biological tissues at 980 nm is one order of magnitude higher than at 808 nm [35]. The water molecules absorb the light at 980 nm and convert it into thermal energy, which can produce a strong thermal effect in local tissues, and then cause local thermal damage, reducing the tissue penetration ability of NIR light [36]. To verify whether the gas storage nanoplatform exhibited good biocompatibility under 808 nm NIR irradiation, we conducted a warming experiment under NIR irradiation, which showed that the rate of temperature increase of UZPA-CP under 808 nm NIR irradiation was much slower (Fig. S9). In addition, we evaluated the risk of tissue damage that might be induced by different wavelengths of NIR. The 980 nm NIR group rapidly increased the mouse skin temperature to about 45 °C after 3 min, whereas the 808 nm NIR group reached about 37 °C only at 9 min (Fig. S10). Therefore, the above results confirmed that the gas storage nanoplatform could effectively avoid the possible overheating effect caused by 980 nm NIR irradiation under 808 nm NIR excitation, and had good biological safety.

3.3. Evaluation of light responsiveness and targeting capabilities of UZPA-CP

After successfully preparing UZPA-CP, we verified its controlled release performance of CO and H_2S under 808 nm NIR irradiation. Firstly, the CO release ability of UZPA-CP under NIR irradiation was quantitatively analyzed, and the results showed that under 808 nm NIR irradiation of 1.5 W cm^{-2}, the release of CO showed a gradual increase, whereas almost no CO released in the control group without NIR irradiation (Fig. 2A). To further demonstrate that UZPA-CP was able to achieve controlled release of CO by 808 nm NIR light, we performed NIR switching experiments, and the results indicated that UZPA-CP consistently released CO during light irradiation and hardly released CO during no light irradiation (Fig. 2B and S11), which was consistent with our designed NIR light-responsive controlled release strategy. Meanwhile, we evaluated the release behavior of H_2S and found that UZPA-CP exhibited good responsiveness and controllability under NIR irradiation and in the presence of CA, similar to that of CO (Fig. 2C and D and S12). Taken together, UZPA-CP successfully achieved the precise and controllable release of dual gases. Due to the relatively short range of action of the gas molecules, we further investigated the cellular uptake behavior of the two gas molecules. We observed H_2S in MC3T3-E1 cells using an H_2S-specific probe (WSP-1) and CO in RAW 264.7 cells using a CO-specific probe (CAY10733). Only in the presence of UZPA-CP and 808 nm NIR irradiation, the uptake behavior of both RAW 264.7 and MC3T3-E1 cells occurred (Fig. 2E and F), indicating that the released CO and H_2S could be efficiently absorbed by the cells.

Given that OP usually affects bones throughout the body, the targeting of UZPA-CP to bone tissues becomes crucial to ensure the effectiveness of its clinical application. Therefore, we evaluated the ability of UZPA-CP to target bone tissue *in vitro* and *in vivo*. Previous study had shown that the phosphonic acid moiety contained in Ald can form a bidentate structure with calcium ions in bone tissue [37], so we employed PA to confer good bone targeting properties to UZPA-CP, thereby enhancing its affinity for bone tissue. Considering that hydroxyapatite (HAP) was the most dominant mineral component in bone tissue [38], we chose HAP to simulate the bone microenvironment. UZPA-CP adsorbed on the surface of HAP was observed by scanning electron microscopy (SEM) at different times to evaluate the affinity of this gas storage nanoplatform for bone tissue. The SEM images showed a gradual increase in the binding of UZPA-CP with HAP with increasing time (Fig. 2G). In contrast, the unmodified UZNP-CP showed almost no nanoparticle binding on the HAP surface (Fig. S13). *In vivo* targeting experiments showed a significant increase in UCL intensity at the spine and femur of mice 6 h after UZPA-CP injection (Fig. 2H). All of these results indicated that UZPA-CP could effectively target bone tissues both *in vivo* and *ex vivo*. The excellent bone targeting property of UZPA-CP is important for its *in vivo* treatment of OP, especially in the treatment of pathological fractures of the spine and femur induced by OP, which can reduce the side effects of overdosage treatment.

3.4. Osteogenic properties

In previous experiments, we verified that UZPA-CP could effectively release H_2S under 808 nm NIR irradiation. Given that H_2S had the ability to promote osteogenic differentiation [39], we used western blot (WB), alkaline phosphatase (ALP) staining, alizarin red (ARS) staining and quantitative reverse transcription-polymerase chain reaction (qRT-PCR) to investigate the osteogenic capacity of the gas storage nanoplatform under 808 nm NIR irradiation. WB results showed that the expression of osteogenic marker proteins, such as osteopontin (OPN) and ALP, was significantly increased in the experimental group (Fig. 3A). ALP was an early indicator for determining the differentiation of osteogenic bone, and the results of ALP staining showed that its activity was highest in the UZPA-CP + NIR group. ARS was a decisive indicator for the formation of mineralized nodules in osteoblasts, the results of ARS staining showed that the mineralized nodules formed by MC3T3-E1 cells were also significantly greater in the UZPA-CP + NIR group than in the other groups, which was in line with the results of the WB assay (Fig. 3B and C). In addition, we also detected the mRNA expression of osteogenesis-related genes by qRT-PCR, such as ALP, bone morphogenetic protein 2 (BMP2), collagen I (COL-1), osteocalcin (OCN), osteopontin (OPN) and RUNX2, and found that the expression of these genes was increased in the UZPA-CP + NIR group (Fig. 3D). The results showed that the UZPA-CP group had difficulty promoting osteoblast differentiation due to the gas release limitations. In addition, no significant changes were observed in the UZPA-C + NIR group, indicating that CO gas had a weak effect on promoting osteogenesis alone. However, UZPA-CP + NIR significantly promoted osteogenic differentiation through the release of CO and H_2S, proving that H_2S gas plays a strong role in the process of promoting osteogenesis. Taken together, these results collectively indicated that UZPA-CP had a significant effect in promoting osteogenic differentiation with the assistance of NIR, showing good osteogenic induction potential.

3.5. Anti-inflammatory capacity in vitro

A prominent pathological feature of osteoporosis is the elevated level of inflammation in bone tissue, and macrophages play an important role in this process in bone immunological studies [40]. As a plastic and pluripotent cell population, macrophages exhibit significant functional differences under the influence or stimulation of different microenvironments, and can be divided into M1-type macrophages that secrete pro-inflammatory cytokines (classically activated macrophages) and

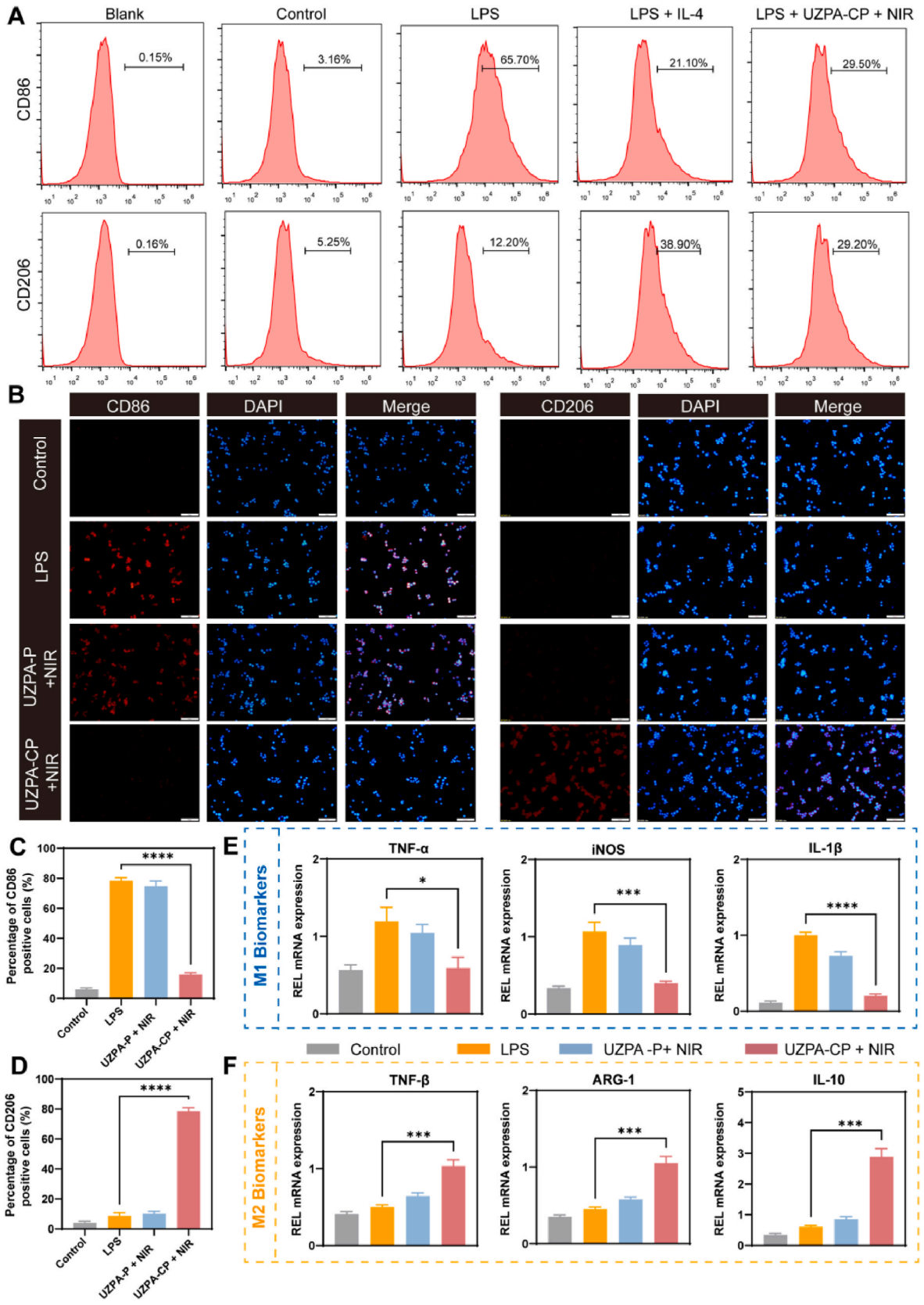

Fig. 4. Immunomodulatory effects of UZPA-CP. (A) Flow cytometry analysis of the expression of CD86 and CD206 in RAW 264.7 cells treated with different treatments. (B) Immunofluorescence images of CD86 and CD206 in RAW 264.7 cells treated with different treatments, scale bar = 50 μm. (C) Quantitative analysis of CD86 in immunofluorescence images. (D) Quantitative analysis of CD206 in immunofluorescence images. (E) mRNA expression levels of M1-type pro-inflammatory cytokines (TNF-α, iNOS and IL-1β) in RAW 264.7 cells treated in different ways. (F) mRNA expression levels of M2-type anti-inflammatory cytokines (TNF-β, ARG-1 and IL-10) in RAW 264.7 cells treated in different ways. Data are mean ± sd (n ≥ 3), $*p < 0.05$, $**p < 0.01$, $***p < 0.001$, $****p < 0.0001$.

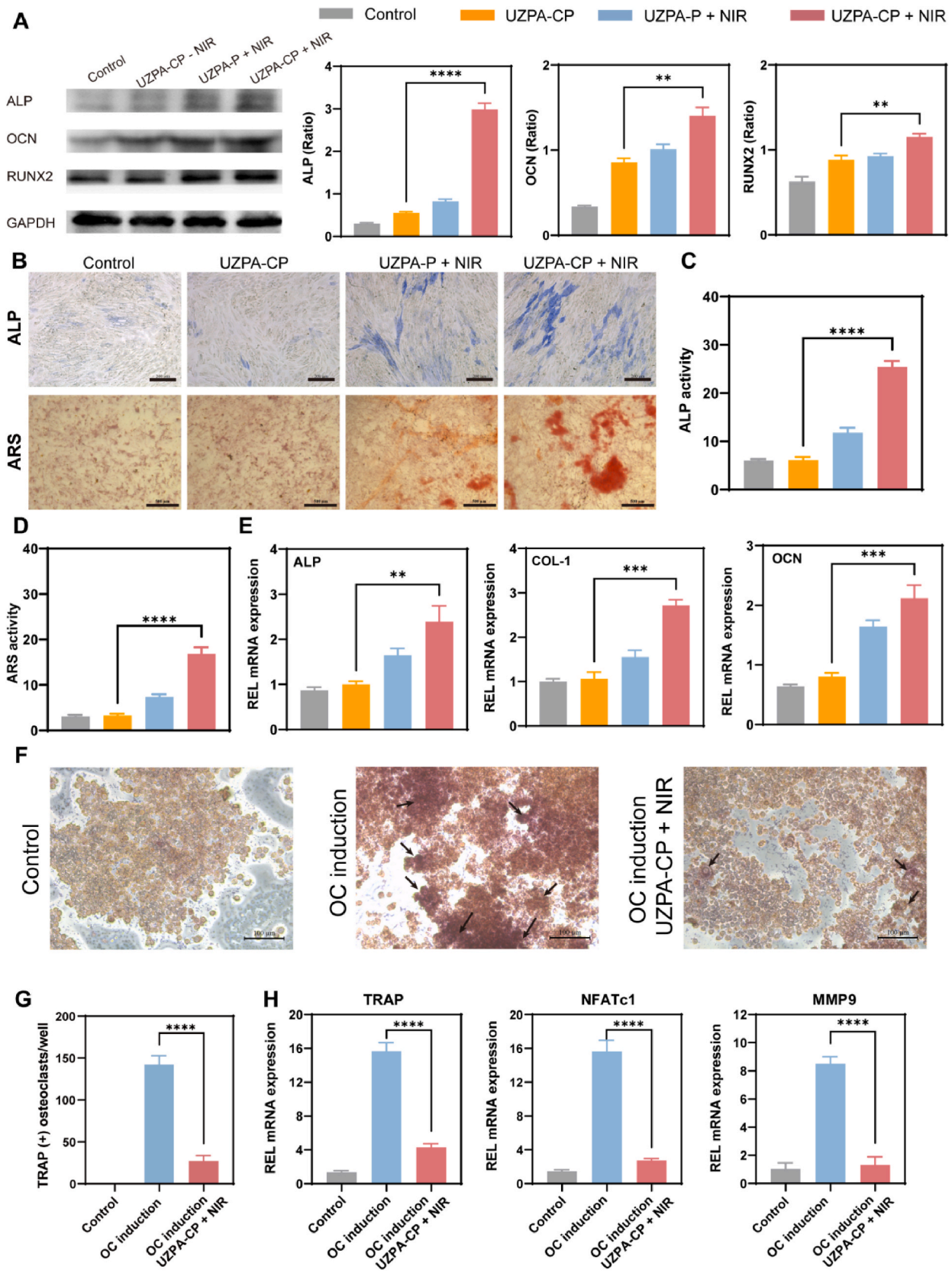

Fig. 5. The role of UZPA-CP in promoting osteogenesis and inhibiting osteoclastogenesis in an inflammatory environment. (A) WB analysis of the protein levels of ALP, OCN and RUNX2 in MC3T3-E1 cells and the corresponding quantitative results of these proteins. (B) ALP staining (scale bar = 200 μm) and ARS staining (scale bar = 500 μm) of MC3T3-E1 cells. (C) Quantitative results corresponding to ALP. (D) Quantitative results corresponding to ARS. (E) mRNA expression of ALP, COL-1 and OCN in MC3T3-E1 cells. (F) Trap staining (scale bar = 100 μm) images after different treatments, with black arrows indicating osteoclasts. (G) Quantitative analysis of the number of TRAP-positive cells. (H) mRNA expression of TRAP, NFATc1 and MMP9 in RAW 264.7 cells treated in different ways. Data are mean ± sd (n ≥ 3), *$p < 0.05$, **$p < 0.01$, ***$p < 0.001$, ****$p < 0.0001$.

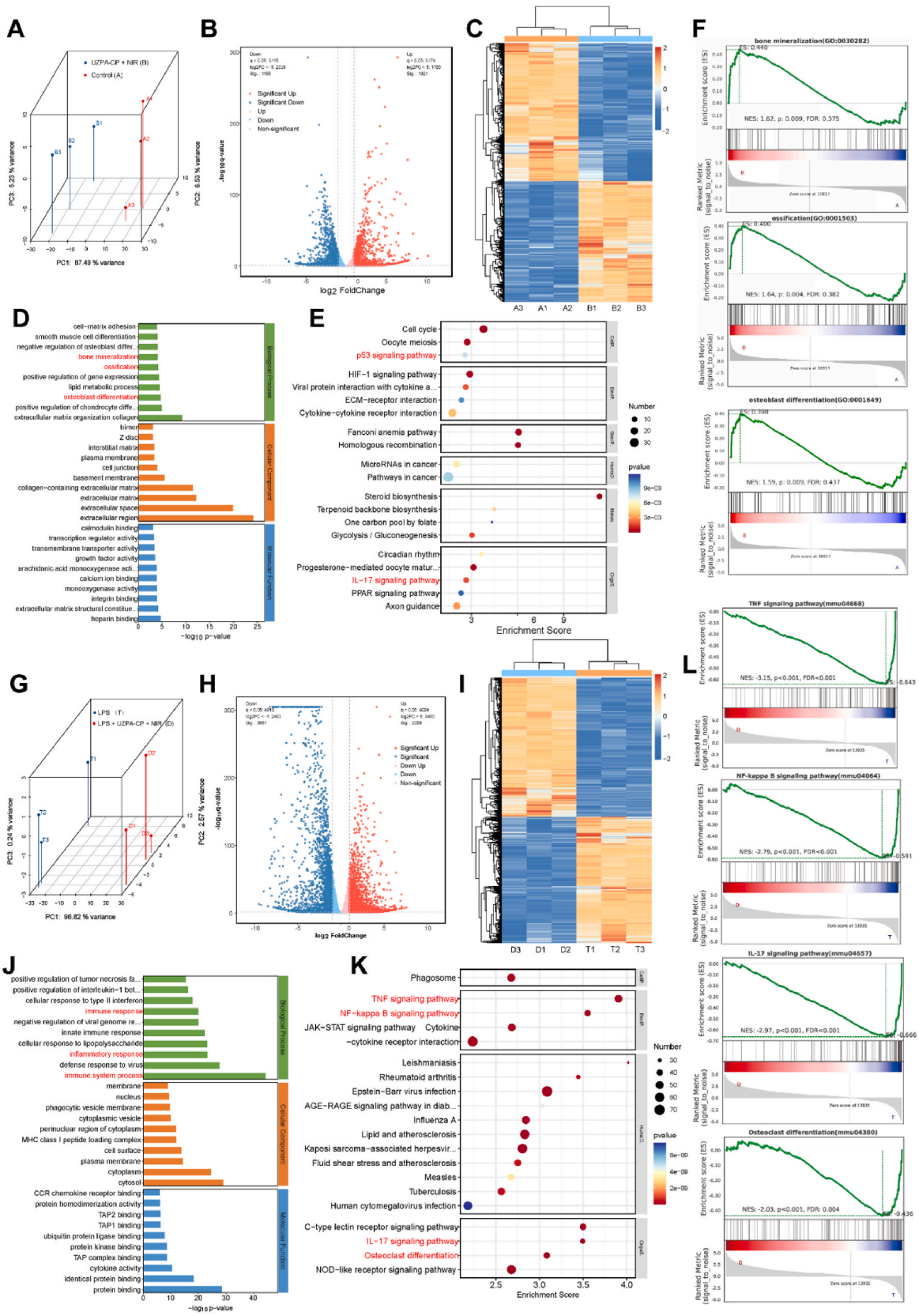

Fig. 6. Anti-inflammatory and pro-osteogenic mechanisms of UZPA-CP. (A) PC analysis of the sequencing results from two groups of MC3T3-E1 cells. (B) Volcano plot displaying upregulated and downregulated genes in MC3T3-E1 cells. (C) Associated heatmap. (D, E) GO analysis and KEGG pathway enrichment analysis. (F) GSE analysis. (G) PC analysis of the sequencing results from two groups of RAW 264.7 cells. (H) Volcano plot displaying upregulated and downregulated genes in RAW 264.7 cells. (I) Associated heatmap. (J, K) GO analysis and KEGG pathway enrichment analysis. (L) GSE analysis.

M2-type macrophages that secrete anti-inflammatory cytokines (alternatively activated macrophages), depending on their activation status [41]. These cells regulate bone homeostasis by secreting associated factors. Once the macrophage polarization is imbalanced, the resulting immune dysregulation causes an inflammatory stimulus that releases a large number of inflammatory factors affecting bone metabolism, leading to further progression of osteoporosis [42].

In this study, RAW 264.7 cells were chosen to evaluate the modulation of inflammation by UZPA-CP nanoparticles under NIR irradiation. Flow cytometry results showed that (Fig. 4A), compared with the control group, the treatment with UZPA-CP + NIR not only significantly reduced the expression of the M1 phenotype marker (CD86) but also increased the expression of M2 macrophage marker (CD206). The polarization state of macrophages under LPS stimulation was evaluated by immunofluorescence staining. The results indicated that the CD86-positive cells significantly increased in the LPS group, confirming that the addition of LPS successfully established an inflammatory microenvironment. In contrast, in the UZPA-CP + NIR group, the fluorescence signal of CD86 was significantly reduced, and the fluorescence signal of CD206 was markedly increased (Fig. 4B–D). In addition, mRNA expression of pro-inflammatory factors (TNF-α, iNOS and IL-1β) and anti-inflammatory factors (TNF-β, ARG-1 and IL-10) was detected by qRT-PCR in each group. The results showed that the UZPA-CP + NIR group significantly inhibited the expression of pro-inflammatory factors while promoting the expression of anti-inflammatory factors (Fig. 4E and F), consistent with the results of flow cytometry and immunofluorescence staining. The results collectively indicated that UZPA-P + NIR could alleviate inflammation to some extent by releasing H_2S, while UZPA-CP + NIR showed significant anti-inflammatory effects by releasing both CO and H_2S, indicating that the released CO had a better effect in regulating the immune microenvironment. Combined with H_2S, it could regulate macrophage polarization, thereby alleviating inflammation by modulating the immune microenvironment, showing good anti-inflammatory potential.

3.6. The ability to promote osteogenesis in an inflammatory environment and inhibit osteoclastogenesis in vitro

During the development of OP, the involvement of immune cells and inflammatory mediators often leads to a disruption of bone tissue homeostasis, resulting in an imbalance between osteoblasts and osteoclasts, which in turn leads to decreased bone formation and increased bone resorption [43]. Therefore, the present study further investigated the effect of this gas storage nanoplatform on the osteogenic process in the presence of NIR in an inflammatory environment. WB assay showed that the expression of osteogenesis-related proteins (ALP, OCN and RUNX2) was significantly increased by the treatment of UZPA-CP + NIR (Fig. 5A). ALP staining and ARS staining results also showed the same trend (Fig. 5B–D). qRT-PCR assay showed a significant increase in the expression levels of osteogenesis-related genes (ALP, COL-1 and OCN) (Fig. 5E). The results collectively indicated that UZPA-CP could not exert effects due to the difficulty in releasing gas. UZPA-P + NIR could promote osteoblast differentiation in an inflammatory environment to a limited extent by releasing H2S. In contrast, UZPA-CP, with the aid of NIR, could significantly promote osteoblast differentiation in an inflammatory environment by releasing CO and H2S, indicating that CO played a good anti-inflammatory and osteogenesis-promoting role in this process. Therefore, UZPA-CP + NIR could alleviate the inhibitory effect on osteoblasts in an inflammatory state, showing good anti-inflammatory and osteogenesis-promoting potential.

Osteoclasts, formed by the fusion of precursor cells of the monocyte/macrophage lineage, are usually generated under the stimulation of nuclear factor κB ligand-receptor activator (RANKL) [44]. In OP, a chronic inflammatory background and a persistent state of immune system hypoactivation promote an inflammatory state in which various types of inflammatory mediators induce the expression of macrophage colony-stimulating factor (M-CSF) and nuclear factor RANKL, which in turn stimulate the formation of osteoclasts [45]. Dysregulation of the balance between osteoclast-driven bone resorption and osteoblast-mediated bone formation is the main pathogenesis of OP. Therefore, this study focused on exploring the effect of this gas storage nanoplatform on osteoclastogenesis. We used RANKL and M-CSF to induce the differentiation of RAW 264.7 cells to osteoclasts, and anti-tartrate acid phosphatase (TRAP) staining and qRT-PCR methods to assess osteoclast formation as a means of investigating the effects of different materials on osteoclast formation. The experimental results showed that some osteoclasts with burgundy-stained cytoplasm were formed in the presence of osteoclast-inducing medium (OC-induced, containing RANKL and M-CSF), whereas the number of osteoclasts was significantly reduced in the UZPA-CP + NIR group (Fig. 5F). The results of the quantitative analysis confirmed the effect of UZPA-CP in inhibiting osteoclast formation *in vitro* (Fig. 5G). In addition, gene expression of osteoclast markers was further detected by qRT-PCR, and it was found that the treatment of NIR-driven UZPA-CP suppressed the expression of osteoclast-related genes, such as matrix metallopeptidase 9 (MMP9), nuclear factor of activated T cells 1 (NFATc1) and TRAP, at the mRNA level (Fig. 5H). These experimental results suggested that this gas storage nanoplatform had an inhibitory effect on osteoclast activity under the control of NIR.

3.7. Molecular mechanisms of UZPA-CP involved in bone formation and anti-inflammatory processes

We further studied the osteogenesis-promoting and anti-inflammatory molecular mechanisms of UZPA-CP under NIR irradiation. Total RNA was extracted from the cells of the control group and the UZPA-CP + NIR group for high-throughput sequencing. Principal component (PC) analysis (Fig. 6A and S14) showed that the homogeneity of the individual groups was satisfactory, but there were significant differences between the different groups, and the samples from both groups met the quality control requirements. Volcano grams and thermograms (Fig. 6B and C) showed significant differences in gene expression between the two groups, with 1021 genes significantly up-regulated and 1168 genes significantly down-regulated in the UZPA-CP + NIR group. Gene ontology (GO) analysis (Fig. 6D) and Kyoto Encyclopedia of Genes and Genomes (KEGG) analysis (Fig. 6E) of these differentially expressed genes showed that these genes were enriched in the pathways of bone mineralization, ossification and osteoblast differentiation, and were significantly correlated with the p53 and IL-17 signaling pathways. Among these, the p53 signaling pathway was associated with the onset of apoptosis, while the IL-17 pathway was associated with inflammation. To confirm the expression status of these pathways, gene set enrichment (GSE) analysis showed that the incorporation of UZPA-CP was negatively correlated with the expression of the p53 signaling pathway and the IL-17 signaling pathway, and positively correlated with the expression of genes related to bone mineralization, ossification, and osteoclast differentiation (Fig. 6F and S15). The above results indicated that the addition of UZPA-CP combined with NIR irradiation suppressed the expression of apoptosis and inflammation-related pathways in MC3T3-E1 and promoted the expression of osteogenesis-related genes.

Next, RAW 264.7 cells were treated with different treatments to explore its anti-inflammation-related mechanism. Among them, the control group was treated with LPS, while the experimental group was treated with UZPA-CP + NIR after the addition of LPS. Subsequently, we collected RNA for sequencing and bioinformatics analysis. PC analyses (Fig. 6G and S16) showed that good homogeneity was maintained within the individual groups, and the samples of both groups met the quality control requirements. Volcano and heat maps showed (Fig. 6H and I) that there were significant differences in gene expression between groups, with 2269 genes significantly up-regulated and 2061 genes significantly down-regulated in the LPS + UZPA-CP + NIR group

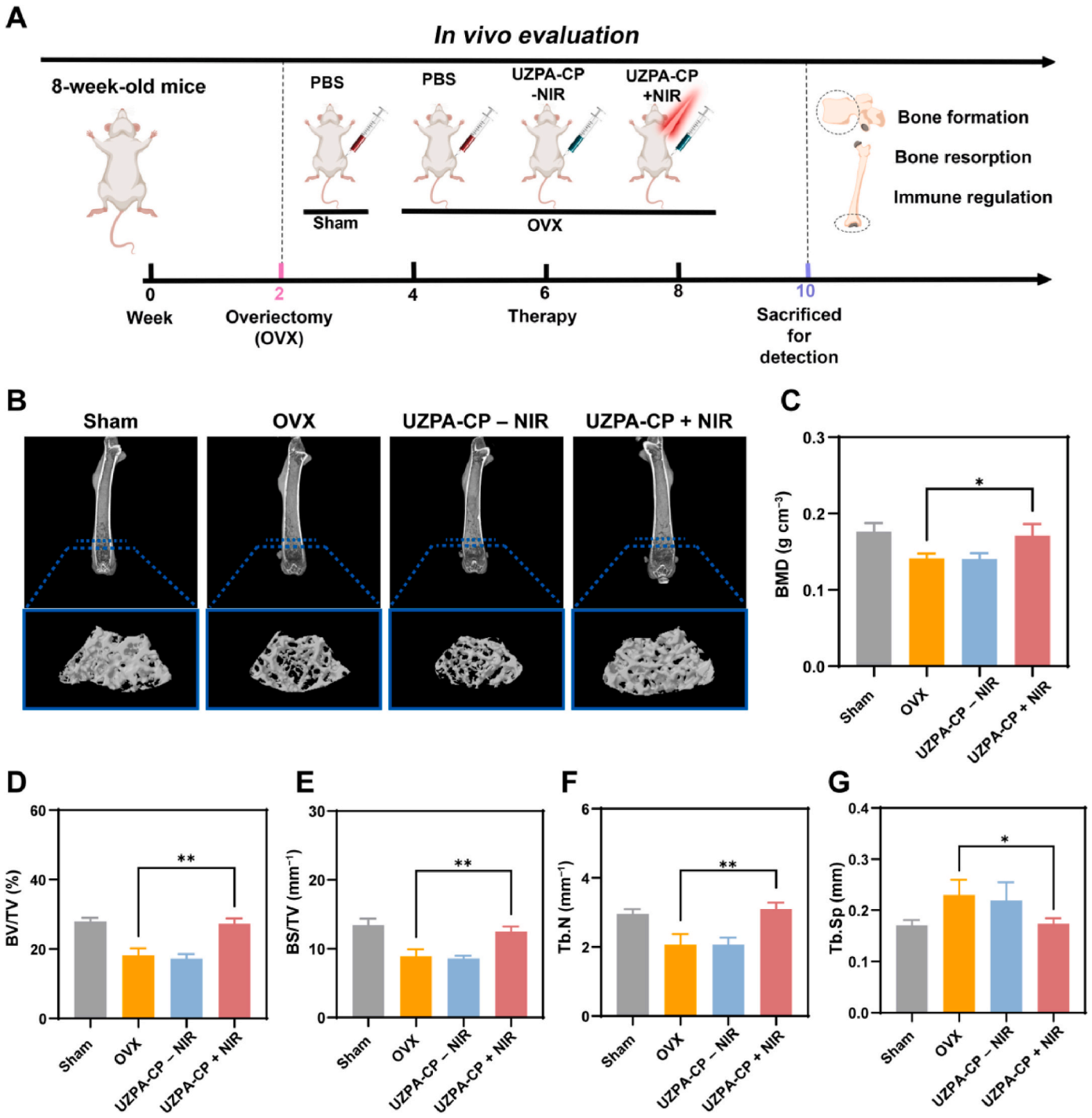

Fig. 7. The therapeutic effect of UZPA-CP on a mouse model of OP. (A) Schematic diagram of the *in vivo* experimental plan, including the establishment of the OP model, treatment process, and efficacy evaluation. (B) Micro-CT images of the distal femoral trabecular microstructure of each group after treatment. (C) Quantitative analysis of BMD parameters of each group after treatment. (D–G) Quantitative analysis of BV/TV, BS/TV, Tb.N and Tb.Sp parameters of the distal femur of each group after treatment. Data are mean ± sd (n = 6), $^{*}p < 0.05$, $^{**}p < 0.01$.

compared with the LPS group. GO analysis (Fig. 6J) showed that the differentially expressed genes were mainly associated with immune system processes and inflammatory responses. KEGG analysis (Fig. 6K) showed that the differentially expressed genes were significantly associated with signaling pathways such as TNF, NF-kappa B, IL-17 and osteoclast differentiation, all of which were closely related to the development of inflammation. The expression status of these pathways was further confirmed by GSE analysis (Fig. 6L). Therefore, it could be concluded that UZPA-CP + NIR effectively suppressed the expression of pathways related to inflammatory response and osteoclast differentiation in RAW 264.7 cells, suggesting its potential role in regulating immune response and controlling inflammation. In summary, this gas storage nanoplatform could inhibit the expression of inflammatory response, inhibit osteoclast formation, and enhance osteoblast osteogenesis with the assistance of NIR, which had the potential to the treatment of OP.

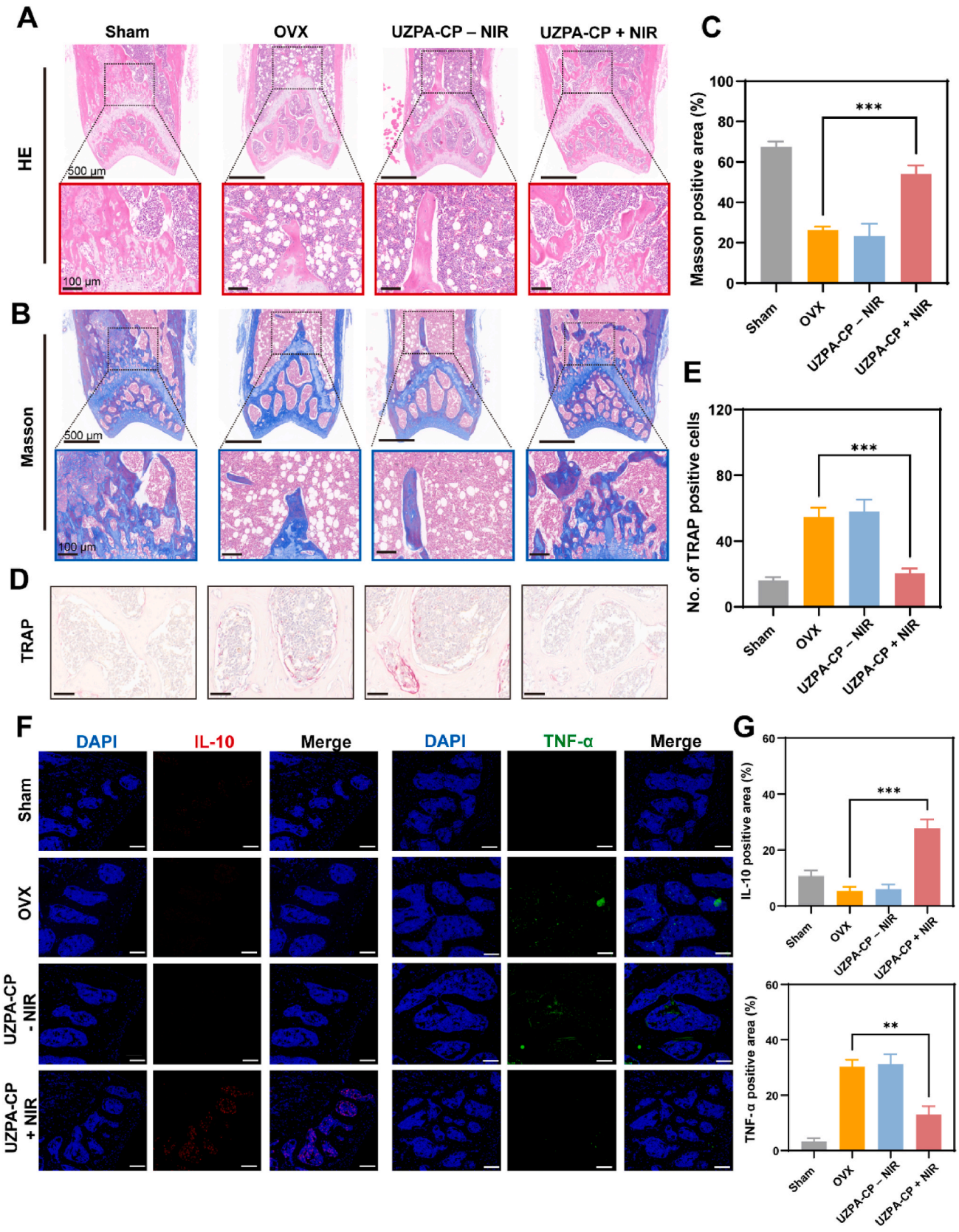

Fig. 8. Histological staining of mice femora. (A) HE staining of the distal femur of mice. (B) Masson's trichrome staining of the distal femur of mice. (C) Quantitative results of the ratio of the new bone area to the total bone area in Masson's trichrome staining. (D) TRAP staining of the distal femur of mice, scale bar = 50 μm. (E) Quantitative analysis of TRAP-positive cells in staining. (F) Immunofluorescence staining images of IL-10 and TNF-α in the distal femur of mice, scale bar = 100 μm. (G) Quantitative analysis of IL-10 and TNF-α in immunofluorescence staining. Data are mean ± sd (n = 6), $^{**}p < 0.01$, $^{***}p < 0.001$.

3.8. In vivo treatment of osteoporosis

To confirm the feasibility of *in vivo* application of this gas storage nanoplatform, we validated its biosafety in mice. Hematoxylin-eosin (HE) staining of major organs (heart, liver, spleen, lung and kidney) (Fig. S17) showed that no significant abnormalities were detected in the UZPA-CP + NIR group compared with the sham-operated (Sham) group, which further validated its good biosafety *in vivo*.

In view of the effects of UZPA-CP in promoting osteogenic differentiation, modulating the immune response and inhibiting the formation of osteoclasts shown *in vitro*, we further investigated the reversal of bone loss in OP by UZPA-CP + NIR in a mouse model of OP established by ovariectomy (OVX) [46]. As shown in the experimental design, mice with ovaries preserved and peripheral fat removed were set up as the Sham group, and OVX mice were divided into the OVX group, the OVX + UZPA-CP – NIR group and the OVX + UZPA-CP + NIR group (Fig. 7A). On the last day of the treatment, all mice were euthanized, and bone quality analysis of the distal femur of the mice was performed using micro-computed tomography (micro-CT). The bone mass was significantly reduced in the OVX group compared with the Sham group and significantly higher in the UZPA-CP + NIR group than in the other groups (except the Sham group) (Fig. 7B), which preliminarily confirmed the efficacy of the bone-targeted gas-storage nanoplatforms for the treatment of OP with NIR intervention. Meanwhile, compared with the Sham group, significant changes in bone microstructural parameters were observed in the OVX group (Fig. 7C–G). Specifically, there was a decrease in bone mineral density (BMD), bone volume to tissue volume ratio (BV/TV), bone surface to tissue volume ratio (BS/TV) and number of trabeculae (Tb.N), while the trabecular separation (Tb.Sp) significantly increased. These indicated that the osteoporosis model had been successfully established. The mice under UZPA-CP + NIR treatment were significantly better than the other experimental groups in the indexes of BMD, BV/TV, BS/TV and Tb.N, and significantly lower than the other experimental groups in Tb.Sp, which proved that UZPA-CP combined with NIR irradiation effectively promoted bone formation *in vivo*, and had a significant therapeutic effect on OP.

To further evaluate the effect of UZPA-CP + NIR in the treatment of OP, we performed histological staining on the treated lumbar vertebrae and femur samples. The results of HE staining and Masson staining of the femur showed that the treatment with UZPA-CP + NIR effectively restored the bone volume and structure of the femur in OVX mice (Fig. 8A–C), and the staining results of the lumbar vertebrae samples showed the same trend (Fig. S18), which further confirmed the effect of UZPA-CP + NIR in restoring the bone volume and structure. The results of TRAP staining showed that the number of osteoclasts (TRAP-positive cells) was increased in mice in the OVX group compared with the Sham group, whereas the UZPA-CP + NIR treatment significantly inhibited the formation of osteoclasts (Fig. 8D and E), consistent with the results of the *in vitro* experiments.

The development of OP is usually associated with chronic inflammation, accompanied by macrophage polarization towards the M1-type [47]. Immunofluorescence staining results and corresponding quantitative results showed that after UZPA-CP + NIR treatment, the IL-10 positive area was significantly increased, while the TNF-α positive area was significantly decreased (Fig. 8F and G), indicating that UZPA-CP + NIR treatment effectively inhibited the polarization of the M1-type macrophages and promoted the M2-type polarization, which significantly reduced the inflammation level of the bone tissue and created a favorable microenvironment for bone regeneration. Taken together, the combination of UZPA-CP and NIR could be expected to achieve the reversal of osteoporosis by reducing the level of inflammation, promoting osteogenic differentiation and inhibiting the formation of osteoclasts.

4. Conclusion

In summary, UZPA-CP, a targeted gas storage nanoplatform for bone tissue, was developed for the first time, and the precise delivery of CO and H_2S to the bone microenvironment was achieved by NIR control. In this study, it was found that H_2S released from UZPA-CP enhanced osteoblast differentiation and CO inhibited osteoclast activity. Moreover, the combination of CO and H_2S effectively promoted the transition of macrophages to an anti-inflammatory M2 phenotype, leading to improved osteogenic processes by modulating the inflammatory microenvironment in OP. Of particular interest was that the COS produced by PhotoTcm under NIR irradiation could further reduce the destruction of bone tissue by osteoclasts by depleting CA secreted by osteoclasts. However, the specific mechanism of action of this gas storage nanoplatform in a co-culture system involving macrophages, osteoblasts and osteoclasts needs to be thoroughly investigated. In addition, future studies should further improve the loading efficiency of the gas storage material to reduce the frequency of endogenous gas administration. Meanwhile, the long-term biosafety and metabolic mechanisms of the gas storage nanoplatform also need to be further investigated. Taken together, this dual-gas-carrying bone-targeting nano-generator shows multiple effects in promoting osteogenesis, inhibiting osteoclastogenesis and improving the immune microenvironment, which provides a new strategy in the treatment of OP, and also provides new perspectives for the design and development of nanomaterials for the treatment of orthopedic and other diseases, such as osteoporotic bone defects and periodontitis.

CRediT authorship contribution statement

Guoyu Yang: Writing – review & editing, Writing – original draft, Validation, Methodology, Investigation, Formal analysis, Data curation. **Jing Ye:** Validation, Investigation, Data curation. **Jingcheng Wang:** Resources, Methodology. **Huijie Liu:** Supervision, Resources, Methodology. **Yanli Long:** Resources, Methodology. **Junkai Jiang:** Writing – review & editing. **Xinxin Miao:** Supervision, Resources. **Jianjian Deng:** Methodology. **Tianlong Wu:** Methodology. **Tao Li:** Methodology. **Xigao Cheng:** Writing – review & editing, Supervision, Resources, Funding acquisition. **Xiaolei Wang:** Writing – review & editing, Supervision, Resources, Funding acquisition.

Declaration of competing interest

The authors declare that they have no known competing financial interests or personal relationships that could have appeared to influence the work reported in this paper.

Data availability

Data will be made available on request.

Acknowledgments

This work was funded by the thousand Talents Program of Jiangxi Province (JXSQ2019201026 to Xigao Cheng), the Scientific and Technological Cooperation Project of Jiangxi Province (20232BBH80001 to Xigao Cheng), Jiangxi Provincial Key Laboratory of Spine and Spinal Cord Disease (2024SSY06131 to Xigao Cheng), the Natural Science Foundation of China (82360424 to Jing Ye), the Natural Science Foundation of Jiangxi Province (20224BAB216031 to Jing Ye), the Natural Science Foundation of Jiangxi Province (20224BAB216032 to Xinxin Miao) and the Key Research and Development Program of Jiangxi Province (20212BBG73004 to Xiaolei Wang).

Appendix A. Supplementary data

Supplementary data to this article can be found online at https://doi.org/10.1016/j.mtbio.2024.101179.

References

[1] I. Foessl, H.P. Dimai, B. Obermayer-Pietsch, Long-term and sequential treatment for osteoporosis, Nat. Rev. Endocrinol. 19 (9) (2023) 520–533, https://doi.org/10.1038/s41574-023-00866-9.

[2] G. Chen, C. Long, S. Wang, Z. Wang, X. Chen, W. Tang, X. He, Z. Bao, B. Tan, J. Zhao, Y. Xie, Z. Li, D. Yang, G. Xiao, S. Peng, Circular rna circstag1 promotes bone regeneration by interacting with hur, Bone Res 10 (1) (2022) 32, https://doi.org/10.1038/s41413-022-00208-x.

[3] F. Huang, P. Wong, J. Li, Z. Lv, L. Xu, G. Zhu, M. He, Y. Luo, Osteoimmunology: the correlation between osteoclasts and the th17/treg balance in osteoporosis, J. Cell Mol. Med. 26 (13) (2022) 3591–3597, https://doi.org/10.1111/jcmm.17399.

[4] L. Zhu, Y. Tang, X.-Y. Li, E.T. Keller, J. Yang, J.-S. Cho, T.Y. Feinberg, S.J. Weiss, Osteoclast-mediated bone resorption is controlled by a compensatory network of secreted and membrane-tethered metalloproteinases, Sci. Transl. Med. 12 (529) (2020), https://doi.org/10.1126/scitranslmed.aaw6143 eaaw6143.

[5] B. Faulkner, K. Astleford, K.C. Mansky, Regulation of osteoclast differentiation and skeletal maintenance by histone deacetylases, Molecules 24 (7) (2019) 1355, https://doi.org/10.3390/molecules24071355.

[6] H. Tamura, T. Maekawa, H. Domon, K. Sirisereephap, T. Isono, S. Hirayama, T. Hiyoshi, K. Sasagawa, F. Takizawa, T. Maeda, Y. Terao, K. Tabeta, Erythromycin restores osteoblast differentiation and osteogenesis suppressed by porphyromonas gingivalis lipopolysaccharide, Pharmaceuticals 16 (2) (2023) 303, https://doi.org/10.3390/ph16020303.

[7] T. Chen, T. Yang, W. Zhang, J. Shao, The therapeutic potential of mesenchymal stem cells in treating osteoporosis, Biol. Res. 54 (1) (2021) 42, https://doi.org/10.1186/s40659-021-00366-y.

[8] A. Kalinkovich, G. Livshits, Biased and allosteric modulation of bone cell-expressing G protein-coupled receptors as a novel approach to osteoporosis therapy, Pharmacol. Res. 171 (2021) 105794, https://doi.org/10.1016/j.phrs.2021.105794.

[9] Y. Zhao, H. Kang, X. Wu, P. Zhuang, R. Tu, T. Goto, F. Li, H. Dai, Multifunctional scaffold for osteoporotic pathophysiological microenvironment improvement and vascularized bone defect regeneration, Adv. Healthcare Mater. 12 (15) (2023) 2203099, https://doi.org/10.1002/adhm.202203099.

[10] H. Zhu, K. Zheng, A.R. Boccaccini, Multi-functional silica-based mesoporous materials for simultaneous delivery of biologically active ions and therapeutic biomolecules, Acta Biomater. 129 (2021) 1–17, https://doi.org/10.1016/j.actbio.2021.05.007.

[11] Y. Huang, M. Chen, Y. Shen, X. Shen, M. Li, Y. Li, Y. Liu, K. Cai, Z. Luo, Y. Hu, Bone-targeting cell membrane-engineered CaCO3-based nanoparticles restore local bone homeostasis for microenvironment-responsive osteoporosis treatment, Chem. Eng. J. 470 (2023) 144145, https://doi.org/10.1016/j.cej.2023.144145.

[12] J. Sun, W. Wang, X. Hu, X. Zhang, C. Zhu, J. Hu, R. Ma, Local delivery of gaseous signaling molecules for orthopedic disease therapy, J. Nanobiotechnol. 21 (1) (2023) 58, https://doi.org/10.1186/s12951-023-01813-6.

[13] W. Gong, C. Xia, Q. He, Therapeutic gas delivery strategies, WIREs Nanomedicine and Nanobiotechnol. 14 (1) (2022) e1744, https://doi.org/10.1002/wnan.1744.

[14] V. Pathak, K. Roemhild, S. Schipper, N. Groß-Weege, T. Nolte, S. Ruetten, E. M. Buhl, A. El Shafei, M. Weiler, L. Martin, G. Marx, V. Schulz, F. Kiessling, T. Lammers, P. Koczera, Theranostic trigger-responsive carbon monoxide-generating microbubbles, Small 18 (18) (2022) 2200924, https://doi.org/10.1002/smll.202200924.

[15] J.D. Byrne, D. Gallo, H. Boyce, S.L. Becker, K.M. Kezar, A.T. Cotoia, V.R. Feig, A. Lopes, E. Csizmadia, M.S. Longhi, J.S. Lee, H. Kim, A.J. Wentworth, S. Shankar, G. R. Lee, J. Bi, E. Witt, K. Ishida, A. Hayward, J.L.P. Kuosmanen, J. Jenkins, J. Wainer, A. Aragon, K. Wong, C. Steiger, W.R. Jeck, D.E. Bosch, M.C. Coleman, D.R. Spitz, M. Tift, R. Langer, L.E. Otterbein, G. Traverso, Delivery of therapeutic carbon monoxide by gas-entrapping materials, Sci. Transl. Med. 14(651) eabl4135. https://doi.org/10.1126/scitranslmed.abl4135.

[16] X. Zhang, Z. Yuan, J. Wu, Y. He, G. Lu, D. Zhang, Y. Zhao, R. Wu, Y. Lv, K. Cai, S. He, An orally-administered nanotherapeutics with carbon monoxide supplying for inflammatory bowel disease therapy by scavenging oxidative stress and restoring gut immune homeostasis, ACS Nano 17 (21) (2023) 21116–21133, https://doi.org/10.1021/acsnano.3c04819.

[17] J. Li, Z. Su, C. Yu, Y. Yuan, Q. Wu, J. Liu, B. Peng, W. Hu, X. Lu, H. Yu, L. Li, W. Huang, Recent progress in the development of sensing systems for in vivo detection of biological hydrogen sulfide, Dyes Pigm 192 (2021) 109451, https://doi.org/10.1016/j.dyepig.2021.109451.

[18] T. Zhou, W. Liu, H. Lai, Y. Liu, W. Su, Z. Xu, Hydrogen sulfide promotes osteogenesis by modulating macrophage polarization, Int. Immunopharmacol. 115 (2023) 109564, https://doi.org/10.1016/j.intimp.2022.109564.

[19] Y. Huang, H. Li, X. He, X. Yang, L. Li, S. Liu, Z. Zou, K. Wang, J. Liu, Near-infrared photothermal release of hydrogen sulfide from nanocomposite hydrogels for anti-inflammation applications, Chin. Chem. Lett. 31 (3) (2020) 787–791, https://doi.org/10.1016/j.cclet.2019.05.025.

[20] F. Sun, Y. Wang, Q. Wang, X. Wang, P. Yao, W. Feng, Q. Yuan, X. Qi, S. Chen, W. Pu, R. Huang, Q. Dai, J. lv, Q. Wang, W. Shen, P. Xia, D. Zhang, Self-illuminating triggered release of therapeutics from photocleavable nanoprodrug for the targeted treatment of breast cancer, ACS Appl. Mater. Interfaces 14 (7) (2022) 8766–8781, https://doi.org/10.1021/acsami.1c21665.

[21] N. Rosic, M. Climstein, G.M. Boyle, D. Thanh Nguyen, Y. Feng, Exploring mycosporine-like amino acid uv-absorbing natural products for a new generation of environmentally friendly sunscreens, Mar. Drugs 21 (4) (2023) 253.

[22] M. Yang, H. Gong, D. Yang, L. Feng, S. Gai, F. Zhang, H. Ding, F. He, P. Yang, Research progress on rare earth up-conversion and near-infrared II luminescence in biological applications, Chin. Chem. Lett. 35 (2) (2024) 108468, https://doi.org/10.1016/j.cclet.2023.108468.

[23] Y. Zhang, X. Zhu, J. Zhang, Y. Wu, J. Liu, Y. Zhang, Synergistic upconversion photodynamic and photothermal therapy under cold near-infrared excitation, J. Colloid Interface Sci. 600 (2021) 513–529, https://doi.org/10.1016/j.jcis.2021.05.017.

[24] L. Ruan, Y. Zhang, Upconversion perovskite nanocrystal heterostructures with enhanced luminescence and stability by lattice matching, ACS Appl. Mater. Interfaces 13 (43) (2021) 51362–51372, https://doi.org/10.1021/acsami.1c14711.

[25] J. Ye, J. Jiang, Z. Zhou, Z. Weng, Y. Xu, L. Liu, W. Zhang, Y. Yang, J. Luo, X. Wang, Near-infrared light and upconversion nanoparticle defined nitric oxide-based osteoporosis targeting therapy, ACS Nano 15 (8) (2021) 13692–13702, https://doi.org/10.1021/acsnano.1c04974.

[26] M. Qi, X. Li, X. Sun, C. Li, F.R. Tay, M.D. Weir, B. Dong, Y. Zhou, L. Wang, H.H. K. Xu, Novel nanotechnology and near-infrared photodynamic therapy to kill periodontitis-related biofilm pathogens and protect the periodontium, Dent. Mater. 35 (11) (2019) 1665–1681, https://doi.org/10.1016/j.dental.2019.08.115.

[27] S. Liu, Y. Sun, T. Zhang, L. Cao, Z. Zhong, H. Cheng, Q. Wang, Z. Qiu, W. Zhou, X. Wang, Upconversion nanoparticles regulated drug & gas dual-effective nanoplatform for the targeting cooperated therapy of thrombus and anticoagulation, Bioact. Mater. 18 (2022) 91–103, https://doi.org/10.1016/j.bioactmat.2022.03.013.

[28] N.J.J. Johnson, A. Korinek, C. Dong, F.C.J.M. van Veggel, Self-focusing by ostwald ripening: a strategy for layer-by-layer epitaxial growth on upconverting nanocrystals, J. Am. Chem. Soc. 134 (27) (2012) 11068–11071, https://doi.org/10.1021/ja302717u.

[29] A. Dong, X. Ye, J. Chen, Y. Kang, T. Gordon, J.M. Kikkawa, C.B. Murray, A generalized ligand-exchange strategy enabling sequential surface functionalization of colloidal nanocrystals, J. Am. Chem. Soc. 133 (4) (2011) 998–1006, https://doi.org/10.1021/ja108948z.

[30] B. Hu, H. Fang, Z. Huang, W. Huang, L. Huang, H. Liu, F. Lv, W. Huang, X. Wang, An upconversion nanoplatform based multi-effective theatment for Parkinson's disease, Chem. Eng. J. 465 (2023) 142959, https://doi.org/10.1016/j.cej.2023.142959.

[31] C. Sheng, F. Yu, Y. Feng, M. Gao, W. Li, L. Li, J. Zhao, Near-infrared light triggered degradation of metal−organic frameworks for spatiotemporally-controlled protein release, Nano Today 49 (2023) 101821, https://doi.org/10.1016/j.nantod.2023.101821.

[32] Y. Zhao, S.G. Bolton, M.D. Pluth, Light-activated COS/H_2S donation from photocaged thiocarbamates, Org. Lett. 19 (9) (2017) 2278–2281, https://doi.org/10.1021/acs.orglett.7b00808.

[33] O.A. Lipina, Y.V. Baklanova, L.L. Surat, M.A. Melkozerova, A.Y. Chufarov, A. P. Tyutyunnik, V.G. Zubkov, Structural and optical characterization of Tm3+-doped apatite related NaLa9(GeO4)6O2 phosphors, Ceram. Int. 46 (16, Part B) (2020) 26416–26424, https://doi.org/10.1016/j.ceramint.2020.03.225.

[34] J. Jiang, J. Xie, L. Zhou, W. Han, J. Ye, D. Hu, W. Xie, J. Qiu, R. Chen, X. Wang, Near infrared responsive nitric oxide and carbon monoxide nanoplatform for synergistic photodynamic therapy against periodontitis, Chem. Eng. J. 480 (2024) 147850, https://doi.org/10.1016/j.cej.2023.147850.

[35] M. Guo, S. Wang, Q. Guo, B. Hou, T. Yue, D. Ming, B. Zheng, NIR-responsive spatiotemporally controlled cyanobacteria micro-nanodevice for intensity-modulated chemotherapeutics in rheumatoid arthritis, ACS Appl. Mater. Interfaces 13 (16) (2021) 18423–18431, https://doi.org/10.1021/acsami.0c20514.

[36] S. Thangudu, C.-S. Chiang, K. Chu Hwang, 1550 nm light activatable photothermal therapy on multifunctional CuBi2O4 bimetallic particles for treating drug resistance bacteria-infected skin in the NIR-III biological window, J. Colloid Interface Sci. 631 (2023) 1–16, https://doi.org/10.1016/j.jcis.2022.10.143.

[37] K. Li, S. Hu, J. Huang, Y. Shi, W. Lin, X. Liu, W. Mao, C. Wu, C. Pan, Z. Xu, H. Wang, L. Gao, H. Chen, Targeting ROS-induced osteoblast senescence and RANKL production by Prussian blue nanozyme based gene editing platform to reverse osteoporosis, Nano Today 50 (2023) 101839, https://doi.org/10.1016/j.nantod.2023.101839.

[38] Y. Zhang, J. Li, V.H.M. Mouser, N. Roumans, L. Moroni, P. Habibovic, Biomimetic mechanically strong one-dimensional Hydroxyapatite/Poly(d,l-lactide) composite inducing formation of anisotropic collagen matrix, ACS Nano 15 (11) (2021) 17480–17498, https://doi.org/10.1021/acsnano.1c03905.

[39] J. Yu, P. Gao, Y. Yang, D. Peng, X. Zhang, D. Wang, W. Yang, Y. Tang, K. Cai, Promoting osseointegration of titanium by pH-responsive releasing of H_2S and optimizing polarization time for macrophages, Compos. B Eng. 253 (2023) 110554, https://doi.org/10.1016/j.compositesb.2023.110554.

[40] Y. Wang, Q. Wang, Q. Xu, J. Li, F. Zhao, Single-cell RNA sequencing analysis dissected the osteo-immunology microenvironment and revealed key regulators in osteoporosis, Int. Immunopharmacol. 113 (2022) 109302, https://doi.org/10.1016/j.intimp.2022.109302.

[41] S. Kang, A. Kumanogoh, The spectrum of macrophage activation by immunometabolism, Int. Immunol. 32 (7) (2020) 467–473, https://doi.org/10.1093/intimm/dxaa017.

[42] V. Fischer, M. Haffner-Luntzer, Interaction between bone and immune cells: implications for postmenopausal osteoporosis, Semin. Cell Dev. Biol. 123 (2022) 14–21, https://doi.org/10.1016/j.semcdb.2021.05.014.
[43] K. Hu, Z. Shang, X. Yang, Y. Zhang, L. Cao, Macrophage polarization and the regulation of bone immunity in bone homeostasis, J. Inflammation Res. 16 (2023) 3563–3580, https://doi.org/10.2147/jir.S423819.
[44] N. Lampiasi, R. Russo, I. Kireev, O. Strelkova, O. Zhironkina, F. Zito, Osteoclasts differentiation from murine RAW 264.7 cells stimulated by RANKL: timing and behavior, Biology 10 (2) (2021) 117.
[45] A. Ho, B. Ngala, C. Yamada, C. Garcia, C. Duarte, J. Akkaoui, D. Ciolac, A. Nusbaum, W. Kochen, D. Efremova, S. Groppa, L. Nathanson, S. Bissel, A. Oblak, M.A. Kacena, A. Movila, IL-34 exacerbates pathogenic features of Alzheimer's disease and calvaria osteolysis in triple transgenic (3x-Tg) female mice, Biomed. Pharmacother. 166 (2023) 115435, https://doi.org/10.1016/j.biopha.2023.115435.
[46] Y. Jin, B.-H. Zhou, J. Zhao, M.M. Ommati, S. Wang, H.-W. Wang, Fluoride-induced osteoporosis via interfering with the RANKL/RANK/OPG pathway in ovariectomized rats: oophorectomy shifted skeletal fluorosis from osteosclerosis to osteoporosis, Environ. Pollut. 336 (2023) 122407, https://doi.org/10.1016/j.envpol.2023.122407.
[47] X. Chen, S. Wang, X. Zhang, Y. Yu, J. Wang, C. Liu, Dual-function injectable fibrin gel incorporated with sulfated chitosan nanoparticles for rhBMP-2-induced bone regeneration, Appl. Mater. Today 26 (2022) 101347, https://doi.org/10.1016/j.apmt.2021.101347.